A linearized ALE Boundary Element Method for flexible 3D bluff bodies in potential flows: towards application to airship aeroelasticity

Robin Le Mestre, Jean-Sébastien Schotté, Olivier Doaré

To cite this version:

Robin Le Mestre, Jean-Sébastien Schotté, Olivier Doaré. A linearized ALE Boundary Element Method for flexible 3D bluff bodies in potential flows: towards application to airship aeroelasticity. Computer Methods in Applied Mechanics and Engineering, 2022, 392, pp.114624. 10.1016/j.cma.2022.114624 . hal-03578790

A linearized ALE Boundary Element Method for flexible 3D bluff bodies in potential flows: towards application to airship aeroelasticity

Robin Le Mestre[a,b], Jean-Sébastien Schotté[b], Olivier Doaré[a]

[a] *IMSIA, ENSTA Paris, Institut Polytechnique de Paris, 828 Boulevard des Maréchaux, 91120, Palaiseau, France*
[b] *DAAA, ONERA, Université Paris Saclay, F-92322 Châtillon, France*

Abstract

Effects of fluid-structure coupling on the dynamic behavior of flexible airships can be modeled with a potential, incompressible, inviscid flow. A new formalism to study the linear behavior of a fluid-structure interface in a time-dependent ambient flow is introduced. The fluid equations are condensed at the interface with the help of integral equations, which are expressed as a function of the structure variables defined on a time-independent reference configuration with an Arbitrary Lagrangian-Eulerian (ALE) formalism. The features of the Boundary Element Method (BEM) used to solve this problem numerically are exhibited. The approximations of this method associated with both linearization and discretization are quantified to validate the model. A simplified flexible airship test case model is studied to illustrate a practical application of the method.

Keywords: fluid-structure interaction, linear stability analysis, arbitrary-lagrangian-eulerian, boundary element method

Contents

---

*Corresponding author
Email address: `roblm@hotmail.fr` (Robin Le Mestre)

1. Introduction

With the emergence of non-rigid airship projects such as stratospheric platforms, envelopes are getting thinner and more flexible [1]. As a consequence, strong couplings between the structure deformations and the surrounding flowing fluid occur. Research works in this domain aim to predict instabilities such as flutter, that can appear at critical velocity. However, the unsteady coupling of the elastic structure with a surrounding flow remains challenging to predict numerically or experimentally because of the large scale of airships.

To tackle the complex problem of flexible airships fluid-structure interaction, Amiryants et al. [2] simplified the volume geometry as surfaces projected on vertical and horizontal planes. The resulting geometry has been modeled as a lifting surface with the panel method in order to take into account circulation effects of the fluid around the hull and fins. This study showed the possible rise of flutter at high velocities, by coupling of the first modes of the free airship with the flow. Bessert et al. [3] further carried a panel method based on a volume mesh, calculating the static deflection of the airship. Their results showed the non-linear nature of the quasi-steady deformations under certain wind conditions. The static flexible solution was determined more precisely by Liu et al. [4] and Wu et al. [5] using Reynolds-Averaged Navier-Stokes (RANS) methods. This numerical study has been validated with a flexible model in a wind tunnel. However, the cost of RANS calculations is prohibitive for large dynamic fluid-structure coupled problems such as airships [1], hence the need for simplified approaches. Li et al. and Azouz et al. [6, 7] derived analytically the added mass effects associated with the important role of the inertia of the fluid surrounding the accelerated airship. These analytic solutions were obtained by approximating the hull shape as a simpler, regular geometric shape. Moreover, Li et al. calculated the linear interaction of a potential fluid with the structure by using the slender body approximation, on which were superimposed turbulence effects at the fins and the tail of the airship, predicting also a risk of flutter at high wind velocities.

The potential flow hypothesis relies on the fact that the rotational part of the fluid can be neglected (therefore not taking into account viscous effects), enabling to express the velocity field as the gradient of a scalar potential field. This hypothesis is met in practice for airships because of their great lengths [1]. However, viscous phenomena are not negligible locally, at the tail and the fins of the airship for example. Despite the drag forces and circulation phenomena are not captured by the potential approach, these contributions might be taken into account afterwards, superimposing it to the potential solution as done by Li [6]. Potential flows are however interesting to consider as they are easier to solve than viscous flows, especially thanks to the Boundary Element Method (BEM). Riccardi & Bernardis [9] used this method to study the dynamics of rising bubbles. Van Opstal & van Brummelen [10] investigated for their part the large displacements of membranes enclosing fluids such as airbags. The level set approach, which enables to describe the boundary of the domain as the set of roots of a function, has been coupled to the BEM resolution by Tan et al and Garzon et al. [11, 12] to solve multiphase flows (respectively bubbles and waves): such methods are particularly well suited for coupled problems involving large deformations of the interface. Véron et al. [13] solved the interaction between submerged pipes with internal and external flows. All these applications imply large displacements as well as partitioned approaches, meaning that the fluid and solid equations are solved separately and on a new deformed mesh at each time step. This paper introduces a method enabling us to solve the monolithic fluid-structure problem associated with the small movements of a membrane that enables to model the strong coupling between flexible structure vibrations and a surrounding flow. It is implemented numerically using a linearized BEM approach in an ALE framework, which is, to the author's knowledge, a novelty compared to the existing literature: actually, BEM had been used with ALE, but the associated linearized formulation had not been developed, and the linearization of the BEM in the context of potential flows is an original aspect of this work. As a linearized approach, it is particularly well suited for studies in the frequency domain or for stability analysis.

The paper is organized as follows. The expression of the work of the fluid pressure on the structure depending on its movements is derived in section 2. The integral representation of the flow in an Eulerian frame is introduced in order to obtain a formulation condensed at the fluid-structure interface. These integral equations are then expressed using an Arbitrary Lagrangian Eulerian (ALE) formulation, enabling to express the pressure work of the flow with respect to time-independent spatial coordinates. The fluid loads are linearized for small movements around the steady state. In section 3, the linear work of the fluid is determined numerically using the BEM. The aeroelastic model is then obtained by coupling those fluid loads with the structure dynamical behavior. In section 4, the error associated with the numerical approximation, the potential flow theory and the linear approximations is quantified by comparison with analytic results, more accurate numerical simulations and a mesh deformation approach. The fluid-structure coupling method in then applied to the case of an ellipsoidal inflated membrane in section 5. The aeroelastic equations are projected on the *in vacuo* modes of the membrane to reduce the computation cost. The modes of the immersed structure are then calculated, exhibiting an instability induced by the coupling of the flow with the deformations of the structure. A conclusion is given in section 6 and the article is completed by some calculation details in two appendices.

2. Derivation of the potential flow efforts on a moving interface with respect to reference spatial coordinates

The aim of this section is to introduce the mathematical fluid model that will be solved numerically using the method presented in the next section. In all the following mathematical derivations, the vectors will be in bold notation and the tensors will be double-struck.

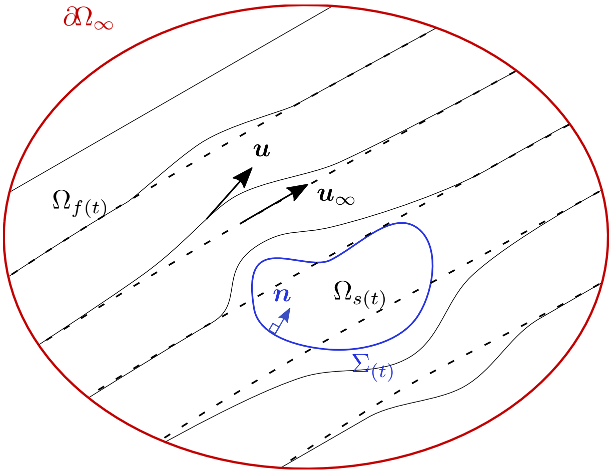

Figure 1: Schematic view of a solid defined by the volume $\Omega_{s(t)}$ that deforms in a flow defined by the volume $\Omega_{f(t)}$. The exterior boundary of the fluid, denoted Ω_∞, is supposed to be at infinity. The ambient flow in absence of solid is supposed to be a homogeneous flow $\boldsymbol{u}_\infty$.

Let us consider a solid ($\Omega_{s(t)}$ domain) that deforms in a potential flow ($\Omega_{f(t)}$ domain), as sketched in Figure 1. The time is denoted t, and the displacement field of the solid is denoted $\boldsymbol{\xi}$. We suppose that this elastic structure is characterized by a stiffness and a mass operator, respectively K_s and M_s. Using a variational approach with $\delta\boldsymbol{\xi}$ a virtual admissible displacement and f_{ext} the work of the external forces on the structure, the weak form of the fluid-structure equation can be written in this form:

$$K_s(\boldsymbol{\xi}, \delta\boldsymbol{\xi}) + M_s\left(\frac{\partial^2\boldsymbol{\xi}}{\partial t^2}, \delta\boldsymbol{\xi}\right) - f_{ext}(\delta\boldsymbol{\xi}) = 0. \tag{1}$$

Under the hypothesis that both Reynolds and Stokes [1] numbers are large:

$$\mathcal{R}_e = \frac{\rho_f U_\infty L}{\mu} \gg 1 \text{ and } \mathcal{S}_t = \frac{\rho_f \Omega L^2}{\mu} \gg 1, \tag{2}$$

---

[1] ratio between inertia and viscosity effects of the fluid

where L and Ω are respectively the characteristic length and circular frequency of the structure, ρ_f and μ are respectively the density and the viscosity of the fluid, and $U_\infty = \|\boldsymbol{u}_\infty\|$ is the characteristic velocity of the ambient flow. Assumption (2) enables to neglect viscosity effects and to use an inviscid fluid model. The forcing term f_{ext} applied by an inviscid fluid on the structure writes [14] :

$$f_{ext}(\delta\boldsymbol{\xi}) = \int_{\Sigma_{(t)}} p\boldsymbol{n} \cdot \delta\boldsymbol{\xi}\, \mathrm{d}\Sigma_{(t)}, \tag{3}$$

p being the pressure and $\boldsymbol{n}$ the normal of the fluid-structure interface $\Sigma_{(t)}$ oriented inward the solid. In order to calculate the dynamical solution of equations (1,3) with respect to the structure movements on a reference, stationnary interface, the fluid's and structure's dynamics have to be linearized. The objective of the next section is to obtain a set of linearized fluid equations using an Arbitrary Lagrangian Eulerian (ALE) formulation.

2.1. Eulerian description of a potential flow

A classical approach when modeling fluid dynamics is to use an Eulerian framework in order to study the velocity of particles through a fixed elementary volume contrarily to the Lagrangian framework, which is focused on the material particles. The fluid equations will first be presented in an Eulerian frame for both kinematic and dynamic equations of the potential flow. A fixed fluid domain Ω_∞ is considered, bounded by a closed surface $\partial\Omega_\infty$ which is a sphere of radius r. The ambient flow $\boldsymbol{u}_\infty$ is defined as the flow in the absence of a structure (dashed streamlines of Figure 1). The latter is supposed to be irrotational, stationary and homogeneous, enabling to express it with a potential ϕ_∞ defined up to a spatial constant by

$$\boldsymbol{u}_\infty = \boldsymbol{\nabla}\phi_\infty \quad \text{in } \Omega_\infty. \tag{4}$$

At the scale of airships, the flow velocity is much lower than that of the sound in air c, and the Mach number $\mathcal{M}_a$ verifies

$$\mathcal{M}_a = \frac{U_\infty}{c} < 0.3, \tag{5}$$

which means the flow can be considered as incompressible. For a potential flow, the incompressibility condition writes:

$$\Delta\phi_\infty = 0 \quad \text{in } \Omega_\infty. \tag{6}$$

When a moving structure is introduced, the domain Ω_∞ is divided into fluid and solid sub-domains $\Omega_{f(t)}$ and $\Omega_{s(t)}$ separated by the fluid-structure interface $\Sigma_{(t)}$. The fluid evolves in a domain $\Omega_{f(t)}$ bounded by the fluid-structure interface $\Sigma_{(t)}$ and its exterior boundary $\partial\Omega_\infty$. The effects of the turbulent boundary layer are neglected and we consider the case where no circulation is induced by the interface on the supposedly inviscid flow $\boldsymbol{u}$ (see hypothesis (2)), enabling to express it with a potential ϕ defined up to a spatial constant by

$$\boldsymbol{u} = \boldsymbol{\nabla}\phi \quad \text{in } \Omega_{f(t)} \text{ with } \phi = \phi_\infty + \phi_p \tag{7}$$

The flow $\boldsymbol{u}$ (continuous streamlines of Figure 1) in the fluid domain is decomposed into an ambient flow $\boldsymbol{u}_\infty$ and a potential perturbed flow $\boldsymbol{u}_p = \boldsymbol{\nabla}\phi_p$ such that:

$$\boldsymbol{u} = \boldsymbol{\nabla}\phi_\infty + \boldsymbol{\nabla}\phi_p \quad \text{in } \Omega_{f(t)}. \tag{8}$$

The flow incompressibility combined with (6) and (8) provides

$$\Delta\phi_p = 0 \quad \text{in } \Omega_{f(t)}. \tag{9}$$

Because of hypothesis (2), the fluid is considered inviscid, therefore the kinematic boundary condition is introduced as

$$\boldsymbol{u}\cdot\boldsymbol{n}=\frac{\partial\boldsymbol{\xi}}{\partial t}\cdot\boldsymbol{n}\quad\text{on }\Sigma_{(t)},\tag{10}$$

$\frac{\partial\boldsymbol{\xi}}{\partial t}$ being the velocity of the interface. When combined with (8), equation (10) becomes

$$\boldsymbol{\nabla}\phi_p\cdot\boldsymbol{n}=\left(\frac{\partial\boldsymbol{\xi}}{\partial t}-\boldsymbol{u}_\infty\right)\cdot\boldsymbol{n}\quad\text{on }\Sigma_{(t)}.\tag{11}$$

Since ϕ_p is defined up to a constant, we arbitrarily impose

$$\phi_p(\boldsymbol{x})\to 0\quad\text{on }\partial\Omega_\infty\text{ for }r\to\infty,\tag{12}$$

to ensure the uniqueness of the solution (r is the radius of the enclosing sphere $\partial\Omega_\infty$). The exterior Laplace equation (9) associated with the Neumann condition (11) and the uniqueness condition (12) is a well-posed problem according to Folland [15], which ensures the existence and unicity of its solution ϕ_p. The latter can be written as the sum of single and double layer terms [15], meaning that its rate of decrease at infinity verifies:

$$\phi_p(\boldsymbol{x})=\mathcal{O}\left(r^{-1}\right)\quad\text{on }\partial\Omega_\infty,\tag{13a}$$

$$\boldsymbol{\nabla}\phi_p(\boldsymbol{x})\cdot\boldsymbol{n}=\mathcal{O}\left(r^{-2}\right)\quad\text{on }\partial\Omega_\infty,\tag{13b}$$

$$\frac{\partial\phi(\boldsymbol{x}_\infty)}{\partial t}=\mathcal{O}\left(r^{-1}\right)\quad\text{on }\partial\Omega_\infty\tag{13c}$$

$$r=\|\boldsymbol{x}\|.\tag{13d}$$

One might note that the potential solution ϕ_p might be referred to as a full potential flow as it is irrotational everywhere on the fluid domain [27], unlike quasi-potential flows which are irrotational everywhere in the fluid domain excepted on an infinitely thin vortex sheet generated behind the rear of the body [28]. Unlike quasi-potential flows, stationary full-potential flows do not generate lift on the structure. In order to obtain a well-defined fluid problem, it is necessary to add initial conditions associated with the movements of the interface, such as the Cauchy condition below:

$$\boldsymbol{\xi}(t_{\text{ini}})=\boldsymbol{\xi}_{\text{ini}}\tag{14a}$$

$$\frac{\partial\boldsymbol{\xi}}{\partial t}(t_{\text{ini}})=\boldsymbol{v}_{\text{ini}}.\tag{14b}$$

The pressure p, needed to compute the virtual work f_{ext} of equation (3), is calculated as a function of the kinematic variables of the fluid using the Bernoulli equation for potential flows:

$$\frac{p}{\rho_f}+\frac{\partial\phi}{\partial t}+\frac{1}{2}\boldsymbol{u}^2+gz=C(t),\tag{15}$$

$C(t)$ being an homogeneous time-dependent parameter. The incompressibility of the fluid (5) ensures that ρ_f is homogeneous. In order to determine the constant $C(t)$, the far field condition of the ambient flow is expressed introducing the energy per unit mass Ψ_∞, far from the structure:

$$\frac{p}{\rho_f}+\frac{1}{2}\boldsymbol{u}^2+gz=\Psi_\infty+\frac{\partial\phi(\boldsymbol{x}_\infty)}{\partial t}=\Psi_\infty\quad\text{on }\partial\Omega_\infty.\tag{16}$$

The above expression is valid at each point remote from the structure because of equations (15) and (13c). By introducing Ψ_∞ into the Bernoulli equation (15), one gets:

$$\frac{p}{\rho_f} + \frac{\partial \phi}{\partial t} + \frac{1}{2}\boldsymbol{u}^2 + gz = \Psi_\infty \quad \text{in } \Omega_{f(t)}. \tag{17}$$

It is convenient, for the sake of understanding the underlying physics behind the model, to separate the pressure in two different contributions. As with velocity potential and velocity, pressure is separated into an ambient pressure p_∞ (not to be confused with the pressure at infinity $p(\boldsymbol{x}_\infty)$), which corresponds to the pressure of the fluid in the absence of the structure, and the pressure perturbation p_p induced by the moving structure:

$$p = p_\infty + p_p \text{ with } \frac{p_\infty}{\rho_f} = \Psi_\infty - \frac{\partial \phi_\infty}{\partial t} - \frac{1}{2}U_\infty^2 - gz \tag{18a}$$

$$\frac{p_p}{\rho_f} = -\frac{1}{2}\boldsymbol{u}_p^2 - \boldsymbol{u}_\infty \cdot \boldsymbol{u}_p - \frac{\partial \phi_p}{\partial t}. \tag{18b}$$

The above expression of the pressure will be used in the numerical implementation to separate the ambient and structure perturbation contributions. Thanks to the equations above, the pressure p, which allows to determine the work of the fluid f_{ext}, can be deduced from the perturbation potential ϕ_p and its spatial derivative $\boldsymbol{u}_p$. It is therefore necessary to obtain the perturbation potential ϕ_p whose calculation with the BEM necessitates to exhibit an integral formulation, which is the aim of the next section.

2.2. Arbitrary Lagrangian Eulerian formulation of the boundary integral equations

The calculation of ϕ_p could be achieved by introducing a weak formulation [16] associated to the local equations (9) and (11) in order to use the Finite Element Method (FEM). However this approach would have inconveniences in this particular case. It would require solving the velocity potential at every node of the fluid mesh, which is very costly. Moreover, because the domain is infinite, it would have to be artificially truncated (by meshing only a part of it in practice), introducing artificial confinement effects. Finally, the ALE formulation is convenient to manage the coupling of the structure with the flow, but it requires the introduction of an unknown fluid mesh deformation when used with the FEM [17]. It is not the case with the BEM as the mesh displacement at the interface is the same as the structure displacement. Consequently, a BEM is used here, and an integral equation involving the Green's function is introduced for that purpose. In the case of Laplace's equation (9) in a three-dimension space [21], Green's function G can be defined as

$$\forall \boldsymbol{x}, \boldsymbol{y} \in \Omega_\infty \times \Omega_\infty : \; \Delta_{\boldsymbol{x}} G(\boldsymbol{x}, \boldsymbol{y}) = \delta(\boldsymbol{x} - \boldsymbol{y}) \tag{19a}$$

$$\boldsymbol{\nabla}_{\boldsymbol{x}} G(\boldsymbol{x}, \boldsymbol{y}) = \frac{\boldsymbol{x} - \boldsymbol{y}}{4\pi \left\|\boldsymbol{x} - \boldsymbol{y}\right\|^3} \tag{19b}$$

$$G(\boldsymbol{x}, \boldsymbol{y}) = -\frac{1}{4\pi(\boldsymbol{x} - \boldsymbol{y})}, \tag{19c}$$

where δ denotes the Dirac distribution. Any function written as the sum of G and a field linear with $\boldsymbol{x}$ would also be a fundamental solution of Laplace's equation, but G has the advantage of decaying to zero at infinity. Since $\partial\Omega_\infty \cup \Sigma_{(t)}$ is an enclosing boundary of the fluid volume $\Omega_{f(t)}$ and $\boldsymbol{n}$ is the outward normal of $\Omega_{f(t)}$, the Green identity can be applied as

$$\begin{aligned} \forall \boldsymbol{y} \in \Omega_\infty, \quad & \int_{\Omega_{f(t)}} \Delta_{\boldsymbol{x}} G_{(\boldsymbol{x},\boldsymbol{y})} \phi_{p(\boldsymbol{x})} - \Delta \phi_{p(\boldsymbol{x})} G_{(\boldsymbol{x},\boldsymbol{y})} \mathrm{d}\Omega_{(\boldsymbol{x})} = ... \\ & \oint_{\Sigma_{(t)} \cup \partial\Omega_\infty} \left[\boldsymbol{\nabla}_{\boldsymbol{x}} G_{(\boldsymbol{x},\boldsymbol{y})} \cdot \boldsymbol{n}_{(\boldsymbol{x})} \phi_{p(\boldsymbol{x})} - \boldsymbol{\nabla} \phi_{p(\boldsymbol{x})} \cdot \boldsymbol{n}_{(\boldsymbol{x})} G_{(\boldsymbol{x},\boldsymbol{y})}\right] \mathrm{d}\Sigma_{(\boldsymbol{x})}. \end{aligned} \tag{20}$$

The rate of decay of the potential (13) and of the Green's function (19b), (19c) at infinity enables us to express the integral on border $\partial\Omega_\infty$ from equation (20), recalling that infinitesimal sphere surfaces (with radius r) $\mathrm{d}\Sigma_{(t)}$ are of order $\mathcal{O}\left(r^2\right)$:

$$\begin{aligned}\oint_{\partial\Omega_\infty} \Big[\boldsymbol{\nabla}_{\boldsymbol{x}} G_{(\boldsymbol{x},\boldsymbol{y})} \cdot \boldsymbol{n}_{(\boldsymbol{x})} \phi_{p(\boldsymbol{x})} - \boldsymbol{\nabla}\phi_{p(\boldsymbol{x})} \cdot \boldsymbol{n}_{(\boldsymbol{x})} G_{(\boldsymbol{x},\boldsymbol{y})}\Big] \mathrm{d}\Sigma_{(\boldsymbol{x})} & \\ = \oint_{\partial\Omega_\infty} \Big[\mathcal{O}\left(r^{-2}\right)\mathcal{O}\left(r^{-1}\right) + \mathcal{O}\left(r^{-1}\right)\mathcal{O}\left(r^{-2}\right)\Big]\mathcal{O}\left(r^{2}\right) & \\ = \mathcal{O}\left(r^{-1}\right) \to 0 & \end{aligned} \tag{21}$$

The above equation enables us to neglect the integral on the border $\partial\Omega_\infty$ from equation (20). The following property, taken from [23]:

$$\int_{\Omega_{f(t)}} \Delta_{\boldsymbol{x}} G_{(\boldsymbol{x},\boldsymbol{y})} \phi_{p(\boldsymbol{x})} \mathrm{d}\Omega = \phi_p(\boldsymbol{y}) \left(1 + \oint_{\Sigma_{(t)}} \boldsymbol{\nabla}_{\boldsymbol{x}} G_{(\boldsymbol{x},\boldsymbol{y})} \cdot \boldsymbol{n}_{(\boldsymbol{x})} \mathrm{d}\Sigma_{(\boldsymbol{x})}\right) \quad \forall \boldsymbol{y} \in \Sigma_{(t)}, \tag{22}$$

combined with equations (9) and (20), gives the regularized expression og the Boundary Integral equation

$$\phi_p(\boldsymbol{y}) = \int_{\Sigma_{(t)}} \boldsymbol{\nabla}_{\boldsymbol{x}} G_{(\boldsymbol{x},\boldsymbol{y})} \cdot \boldsymbol{n}_{(\boldsymbol{x})} \left(\phi_{p(\boldsymbol{x})} - \phi_{p(\boldsymbol{y})}\right) + G_{(\boldsymbol{x},\boldsymbol{y})} \left(\boldsymbol{u}_\infty - \frac{\partial \boldsymbol{\xi}_{(\boldsymbol{x})}}{\partial t}\right) \cdot \boldsymbol{n}_{(\boldsymbol{x})} \mathrm{d}\Sigma_{(\boldsymbol{x})} \quad \forall \boldsymbol{y} \in \Sigma_{(t)}. \tag{23}$$

The solution of this equation can be approximated using the BEM. However, since the interface $\Sigma_{(t)}$ is time-dependent, solving such an equation would imply building a new mesh at each time step. In order to calculate the integral representation of the fluid problem by the means of of time-independent space coordinates, the ALE method expresses the parameters of the fluid with respect to a fixed reference interface. The linearized equations will be derived relatively to a reference position $\overline{\Sigma}$, arbitrarily set to be the fluid-structure interface in the absence of deformations: $\overline{\Sigma} = \Sigma_{(\boldsymbol{\xi}=\mathbf{0})}$, see Figure 2. The physical variables evolving on the time-dependent interface $\Sigma_{(t)}$ will then be expressed as a function of the reference interface $\overline{\Sigma}$, as detailed in [17] in the context of elastic structures interacting with viscous flows. The variables defined on $\overline{\Sigma}$ are written with a bar $\overline{(\bullet)}$. The displacement $\bar{\boldsymbol{\xi}}$ of the physical interface at $\boldsymbol{x} \in \Sigma_{(t)}$ is thus decomposed as

$$\bar{\boldsymbol{\xi}}(\bar{\boldsymbol{x}}, t) = \boldsymbol{x}(\bar{\boldsymbol{x}}, t) - \bar{\boldsymbol{x}} \quad \forall \bar{\boldsymbol{x}} \in \overline{\Sigma}. \tag{24}$$

It is the common definition of the displacement in solid mechanics written in a Lagrangian framework (hence inherent to a moving material point). The surface vector gradient $\overline{\boldsymbol{\nabla}}_S$, the surface gradient tensor $\overline{\nabla}_S$, the surface deformation gradient $\overline{\mathbb{F}}_S$ and the surface deformation operator $\bar{\Phi}_S$ are useful tools for the description of the geometrical evolution of the interface, defined as:

$$\overline{\boldsymbol{\nabla}}_S(\bullet) = (\mathbb{1} - \bar{\boldsymbol{n}} \otimes \bar{\boldsymbol{n}})\overline{\boldsymbol{\nabla}}(\bullet), \tag{25a}$$

$$\overline{\nabla}_S^{\mathrm{T}}(\bullet) = (\mathbb{1} - \bar{\boldsymbol{n}} \otimes \bar{\boldsymbol{n}})\overline{\nabla}^{\mathrm{T}}(\bullet), \tag{25b}$$

$$\overline{\mathbb{F}}_S(\bar{\boldsymbol{\xi}}) = \mathbb{1} + \overline{\nabla}_S \bar{\boldsymbol{\xi}}, \tag{25c}$$

$$\bar{\Phi}_S(\bar{\boldsymbol{\xi}}) = \det\left(\overline{\mathbb{F}}_S\left(\bar{\boldsymbol{\xi}}\right)\right)\ \overline{\mathbb{F}}_S(\bar{\boldsymbol{\xi}})^{-1}. \tag{25d}$$

One can express an oriented infinitesimal element of surface $\boldsymbol{n}\mathrm{d}\Sigma$ through the surface deformation operator using Nanson's formula based on the interface deformations, as shown in [21, 19, 20]:

$$\boldsymbol{n}(\boldsymbol{x})\mathrm{d}\Sigma(\boldsymbol{x}) = \bar{\Phi}_S(\bar{\boldsymbol{\xi}})^{\mathrm{T}} \bar{\boldsymbol{n}}(\bar{\boldsymbol{x}})\mathrm{d}\overline{\Sigma}(\bar{\boldsymbol{x}}) \quad \forall \bar{\boldsymbol{x}} \in \overline{\Sigma}, \tag{26}$$

where $\bar{\boldsymbol{n}}\mathrm{d}\overline{\Sigma}$ denotes an infinitesimal oriented area on the reference surface $\overline{\Sigma}$ and superscript $(\bullet)^T$ denotes the transpose of a tensor. Let us remark that we use here the surface deformation operator $\bar{\Phi}_S$ which has the advantage of using the surface gradient of the interface displacement [21], unlike the classical expression of Nanson's formula which requires to know the normal derivative of the interface displacements. The flow velocity potential and velocity with respect to the reference interface are defined as well:

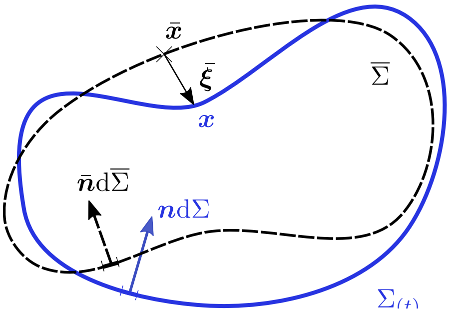

Figure 2: Reference and actual configuration of the problem.

$$\bar{\phi}_p(\bar{\boldsymbol{x}}) \equiv \phi_p(\boldsymbol{x}), \quad \bar{\boldsymbol{u}}_p(\bar{\boldsymbol{x}}) \equiv \boldsymbol{u}_p(\boldsymbol{x}) \quad \forall \bar{\boldsymbol{x}} \in \overline{\Sigma}, \tag{27}$$

where ≡ stands for "is defined as". The Green's function and its normal derivative appearing in (23) are defined similarly:

$$\overline{\boldsymbol{G_n}}_{\left(\bar{\boldsymbol{x}},\bar{\boldsymbol{y}},\bar{\boldsymbol{\xi}}\right)}\mathrm{d}\overline{\Sigma}_{(\bar{\boldsymbol{x}})} \equiv G_{(\boldsymbol{x},\boldsymbol{y})}\boldsymbol{n}_{(x)}\mathrm{d}\Sigma_{(x)} \qquad \forall \bar{\boldsymbol{x}}, \bar{\boldsymbol{y}} \in \overline{\Sigma}, \tag{28a}$$

$$\overline{\partial_n G}_{\left(\bar{\boldsymbol{x}},\bar{\boldsymbol{y}},\bar{\boldsymbol{\xi}}\right)}\mathrm{d}\overline{\Sigma}_{(\bar{\boldsymbol{x}})} \equiv \boldsymbol{\nabla}_x G_{(\boldsymbol{x},\boldsymbol{y})} \cdot \boldsymbol{n}_{(\boldsymbol{x})}\mathrm{d}\Sigma_{(\boldsymbol{x})} \qquad \forall \bar{\boldsymbol{x}}, \bar{\boldsymbol{y}} \in \overline{\Sigma}. \tag{28b}$$

It is worth noticing that equations (24), (27) and (28) differ from (26) as the former ones define an equality between the variables expressed on the physical and reference spaces whereas $\boldsymbol{n}\mathrm{d}\Sigma$ undergoes a transformation relatively to the reference configuration $\bar{\boldsymbol{n}}\mathrm{d}\overline{\Sigma}$. The way $\bar{\phi}_p$ is defined is not inherent to a moving fluid particle contrarily to a Lagrangian framework, but results from their observation on a point moving in space which also differs from the Eulerian framework that observes particles properties on a fixed point of space. This is the reason why this method is referred to as an Arbitrary Lagrangian Eulerian (ALE) approach [22]. By combining (11), (24), (26) and (27) (noting that, for an homogeneous ambient flow, the parameter $\boldsymbol{u}_\infty$ does not vary when it is expressed in the time dependant or in the reference domain), we deduce:

$$G_{(\boldsymbol{x},\boldsymbol{y})}\boldsymbol{\nabla}\phi_{p(\boldsymbol{x})} \cdot \boldsymbol{n}_{(\boldsymbol{x})}\mathrm{d}\Sigma_{(\boldsymbol{x})} = \overline{\boldsymbol{G_n}}_{\left(\bar{\boldsymbol{x}},\bar{\boldsymbol{y}},\bar{\boldsymbol{\xi}}\right)} \cdot \left(\frac{\partial \bar{\boldsymbol{\xi}}_{(\bar{\boldsymbol{x}})}}{\partial t} - \boldsymbol{u}_\infty\right)\mathrm{d}\overline{\Sigma} \quad \forall \bar{\boldsymbol{x}}, \bar{\boldsymbol{y}} \in \overline{\Sigma}. \tag{29}$$

The integral representation (23) written on the reference configuration is then given by:

$$\bar{\phi}_p(\bar{\boldsymbol{y}}) = \int_{\overline{\Sigma}} \overline{\partial_n G}_{\left(\bar{\boldsymbol{x}},\bar{\boldsymbol{y}},\bar{\boldsymbol{\xi}}\right)} \left(\bar{\phi}_{p(\bar{\boldsymbol{x}})} - \bar{\phi}_{p(\bar{\boldsymbol{y}})}\right) + \overline{\boldsymbol{G_n}}_{\left(\bar{\boldsymbol{x}},\bar{\boldsymbol{y}},\bar{\boldsymbol{\xi}}\right)} \cdot \left(\boldsymbol{u}_\infty - \frac{\partial \bar{\boldsymbol{\xi}}_{(\bar{\boldsymbol{x}})}}{\partial t}\right)\mathrm{d}\overline{\Sigma} \quad \forall \bar{\boldsymbol{y}} \in \overline{\Sigma}. \tag{30}$$

Furthermore, we can introduce the time derivative of a scalar function expressed on a moving point of the interface using the chain rule:

$$\frac{\mathrm{d}\bar{\phi}(\bar{\boldsymbol{x}},t)}{\mathrm{d}t} = \frac{\mathrm{d}\phi(\boldsymbol{x},t)}{\mathrm{d}t} = \frac{\partial \phi(\boldsymbol{x})}{\partial t} + \frac{\partial \boldsymbol{x}}{\partial t} \cdot \boldsymbol{\nabla}\phi(\boldsymbol{x}) \quad \forall \bar{\boldsymbol{x}} \in \overline{\Sigma}. \tag{31}$$

By replacing the expression of $\frac{\partial \boldsymbol{x}}{\partial t} = \frac{\partial \boldsymbol{\xi}}{\partial t} = \frac{\partial \bar{\boldsymbol{\xi}}}{\partial t}$ and $\boldsymbol{\nabla}\phi = \boldsymbol{u}(\boldsymbol{x}) = \bar{\boldsymbol{u}}(\bar{\boldsymbol{x}})$, equation (31) becomes:

$$\frac{\partial \phi(\boldsymbol{x},t)}{\partial t} = \frac{\mathrm{d}\bar{\phi}(\bar{\boldsymbol{x}},t)}{\mathrm{d}t} - \frac{\partial \bar{\boldsymbol{\xi}}(\bar{\boldsymbol{x}},t)}{\partial t} \cdot \bar{\boldsymbol{u}}(\bar{\boldsymbol{x}},t) \quad \forall \boldsymbol{x} \in \Sigma. \tag{32}$$

We introduce the pressure $\bar{p}$ with respect to the reference interface:

$$\bar{p}(\bar{\boldsymbol{x}}) \equiv p(\boldsymbol{x}) \quad \forall \bar{\boldsymbol{x}} \in \overline{\Sigma}. \tag{33}$$

By combining equations (17), (32) and (33), we obtain the ALE formulation of the Bernoulli equation:

$$\frac{\bar{p}}{\rho_f} = \Psi_\infty - \frac{1}{2}\bar{\boldsymbol{u}}^2 - \frac{\mathrm{d}\bar{\phi}}{\mathrm{d}t} + \frac{\partial \bar{\boldsymbol{\xi}}}{\partial t} \cdot \bar{\boldsymbol{u}} - g\boldsymbol{e}_z \cdot (\bar{\boldsymbol{x}} + \bar{\boldsymbol{\xi}}) \quad \text{on } \overline{\Sigma}. \tag{34}$$

Finally, equation (34) can be used to express the virtual work of the pressure forces of equation (3) as:

$$f_{ext}(\boldsymbol{\xi}, \delta\boldsymbol{\xi}) = \rho_f \int_{\overline{\Sigma}} \left(\Psi_\infty - \frac{1}{2}\bar{\boldsymbol{u}}^2 - \frac{\mathrm{d}\bar{\phi}}{\mathrm{d}t} + \frac{\partial \bar{\boldsymbol{\xi}}}{\partial t} \cdot \bar{\boldsymbol{u}} - g\boldsymbol{e}_z \cdot (\bar{\boldsymbol{x}} + \bar{\boldsymbol{\xi}}) \right) (\bar{\boldsymbol{\Phi}}_S^{\mathrm{T}} \bar{\boldsymbol{n}}) \cdot \delta\boldsymbol{\xi} \, \mathrm{d}\overline{\Sigma} \tag{35}$$

In the above equation, the terms Ψ_∞, $\bar{\boldsymbol{u}}^2$ and $g\boldsymbol{e}_z \cdot (\bar{\boldsymbol{x}} + \bar{\boldsymbol{\xi}})$ come from the stationary expression of the Bernoulli equation. The time derivative of the potential results from the local acceleration of the fluid, and the scalar product between the structure and the fluid velocity is a convection term linked to the interface movement in an ALE framework. The deformation operator $\bar{\boldsymbol{\Phi}}_S$ enables to take into account the fluctuations (rotation and dilatation) of the oriented interface. A numerical approximation of the set of equations (30) and (35) can be found, but requires to solve different operators at each time step, because of the time dependence of $\overline{\partial_n G}$ and $\overline{\boldsymbol{G}_{\boldsymbol{n}}}$. In order to solve this problem with time-independent operators, a linearized formulation of the integral representation (30) under the assumption of small displacement of the fluid-structure interface $\Sigma_{(t)}$ is introduced in the next subsection.

2.3. Linearized formulation

The linearization of the equations resulting from the combined ALE and BEM approaches is now addressed, under the assumption that the following small perturbations hypotheses are satisfied:

$$\varepsilon = \frac{\max(\|\boldsymbol{\xi}\|)}{L} \ll 1 \text{ and } \|\nabla\boldsymbol{\xi}\| \ll 1. \tag{36}$$

We then develop at order 1 the fluid equations with respect to the small coefficient ε. For conditions (2.3) to be met, the reference configuration $\overline{\Sigma}$ used is the deformed state associated with the stationary flow allowing us to study small perturbations around this equilibrium state, as explained by [17]. If the stress free interface (in the absence of external fluid) was to be used as a reference interface $\overline{\Sigma}$, one would have to check that the steady state deformations induced are of small amplitude before performing the linearization, in order to prevent geometric non-linearities which are not investigated in the present approach. The lack of terms in $\mathcal{O}\left(\varepsilon^2\right)$ to describe the fluid variables leads to an approximation of the solution (quantified in section 4), but it enables to predict the apparition of instabilities [24, 25]. For the sake of conciseness, the terms in $\mathcal{O}\left(\varepsilon\right)$ of the variables (also referred to as the order 1 variables) will be denoted with a $(\bullet)^1$ superscript. The component in $\mathcal{O}\left(\varepsilon^0\right)$ of the variables will be denoted either with a superscript $(\bullet)^0$, or with no superscript when it is implicit because they do not fluctuate with the structure movements. The displacement of the structure then writes:

$$\bar{\boldsymbol{\xi}}^1(\bar{\boldsymbol{x}}) = \boldsymbol{x} - \bar{\boldsymbol{x}} \quad \forall \bar{\boldsymbol{x}} \in \overline{\Sigma}. \tag{37}$$

Because of the small perturbations hypotheses, it is implicit that $\bar{\boldsymbol{\xi}}$ is in $\mathcal{O}\left(\varepsilon\right)$, but the $\bar{\boldsymbol{\xi}}^1$ notation with a superscript is used here to help keeping in mind the condition of small displacements required for the linear formulation. The linearized Nanson's formula (26) can be expressed with $\bar{\boldsymbol{\tau}}^1$ which takes into account both the linear rotation of the normal $\boldsymbol{n}^1$ and the dilatation of the interface [18, 21, 19, 20]:

$$\boldsymbol{n} = \bar{\boldsymbol{n}} + \boldsymbol{n}^1 + \mathcal{O}\left(\varepsilon^2\right) \quad \text{on } \overline{\Sigma} \tag{38a}$$

$$\text{with } \boldsymbol{n}^1 = -\left[\overline{\nabla}_S^{\mathrm{T}} \bar{\boldsymbol{\xi}}^1\right] \bar{\boldsymbol{n}}. \tag{38b}$$

$$\boldsymbol{n}\mathrm{d}\Sigma_{(t)} = \left(\bar{\boldsymbol{n}} + \bar{\boldsymbol{\tau}}^1\right) \overline{\Sigma} + \mathcal{O}\left(\varepsilon^2\right) \quad \text{on } \overline{\Sigma} \tag{38c}$$

$$\text{with } \bar{\boldsymbol{\tau}}^1 = \left(\mathrm{tr}\left(\overline{\nabla}_S \bar{\boldsymbol{\xi}}^1\right) - \overline{\nabla}_S^{\mathrm{T}} \bar{\boldsymbol{\xi}}^1\right) \bar{\boldsymbol{n}} \tag{38d}$$

The Green's function (28), similarly to the method presented by [26], is decomposed in order 0 and 1 terms:

$$\overline{\boldsymbol{G_n}} = \overline{\boldsymbol{G_n}}^0 + \overline{\boldsymbol{G_n}}^1 + \mathcal{O}\left(\varepsilon^2\right) \qquad \text{on } \overline{\Sigma}, \tag{39a}$$

$$\overline{\partial_n G} = \overline{\partial_n G}^0 + \overline{\partial_n G}^1 + \mathcal{O}\left(\varepsilon^2\right) \qquad \text{on } \overline{\Sigma}. \tag{39b}$$

Detailed expressions of (38c) and (39) can be found in Appendix A. The assumption that the structure velocity is small (relatively to the ambient flow U_∞) is also used:

$$\frac{\partial \bar{\boldsymbol{\xi}}^1}{\partial t} = \mathcal{O}\left(\varepsilon\right). \tag{40}$$

Consequently, in the following equations, the superscript $(\bullet)^1$ will not only information on the order 1 amplitude of a variable, but will as well imply its linearity to the displacements $\bar{\boldsymbol{\xi}}^1$ or its time derivatives. Hypothesis (40) is necessary to obtain a movement-independent order 0 solution $\bar{\phi}_p^0$ as it will appear in the integral representation (42). Based on equations (30), (37), (39) and (40), a linearization of the potential $\bar{\phi}_p$ is introduced such that

$$\bar{\phi}_p(\bar{\boldsymbol{x}}) \equiv \phi_p(\boldsymbol{x}) = \bar{\phi}_p^0(\bar{\boldsymbol{x}}) + \bar{\phi}_p^1(\bar{\boldsymbol{x}}) + \mathcal{O}\left(\varepsilon^2\right) \qquad \text{on } \overline{\Sigma}. \tag{41}$$

By first keeping only the terms in $\mathcal{O}\left(1\right)$ from (30), we obtain the order 0 solution described in (42a). Afterwards, the linearization methodology consists in subtracting the order 0 equation (42a) from (30), and by neglecting the contributions in $\mathcal{O}\left(\varepsilon^2\right)$, the order 1 term is solution of (42b):

$$\bar{\phi}_p^0(\bar{\boldsymbol{y}}) = \int_{\overline{\Sigma}} \overline{\partial_n G}^0_{(\bar{\boldsymbol{x}},\bar{\boldsymbol{y}})} \left(\bar{\phi}^0_{p(\bar{\boldsymbol{x}})} - \bar{\phi}^0_{p(\bar{\boldsymbol{y}})}\right) + \overline{\boldsymbol{G_n}}^0_{(\bar{\boldsymbol{x}},\bar{\boldsymbol{y}})} \cdot \boldsymbol{u}_\infty \mathrm{d}\overline{\Sigma} \qquad \forall \bar{\boldsymbol{y}} \in \overline{\Sigma}, \tag{42a}$$

$$\begin{aligned}\bar{\phi}_p^1(\bar{\boldsymbol{y}}) = \int_{\overline{\Sigma}} & \overline{\partial_n G}^0_{(\bar{\boldsymbol{x}},\bar{\boldsymbol{y}})} \left(\bar{\phi}^1_{p(\bar{\boldsymbol{x}})} - \bar{\phi}^1_{p(\bar{\boldsymbol{y}})}\right) + \overline{\partial_n G}^1_{(\bar{\boldsymbol{x}},\bar{\boldsymbol{y}},\bar{\boldsymbol{\xi}}^1)} \left(\bar{\phi}^0_{p(\bar{\boldsymbol{x}})} - \bar{\phi}^0_{p(\bar{\boldsymbol{y}})}\right) \dots \\ & - \overline{\boldsymbol{G_n}}^0_{(\bar{\boldsymbol{x}},\bar{\boldsymbol{y}})} \cdot \frac{\partial \bar{\boldsymbol{\xi}}^1_{(\bar{\boldsymbol{x}})}}{\partial t} + \overline{\boldsymbol{G_n}}^1_{(\bar{\boldsymbol{x}},\bar{\boldsymbol{y}},\bar{\boldsymbol{\xi}}^1)} \cdot \boldsymbol{u}_\infty \mathrm{d}\overline{\Sigma} \qquad \forall \bar{\boldsymbol{y}} \in \overline{\Sigma}.\end{aligned} \tag{42b}$$

The above equations express ϕ_p as a function of variables defined only on the reference configuration. The differentiability of the BEM operators appearing in these equations has already been studied in the field of acoustics [26]. It has been introduced here in the context of incompressible flows. In order to obtain the total linearized velocity potential ϕ, we need to introduce the linearized variations of the ambient potential $\bar{\phi}_\infty$ defined as

$$\bar{\phi}_\infty(\bar{\boldsymbol{x}}) \equiv \phi_\infty(\boldsymbol{x}) = \phi_\infty(\bar{\boldsymbol{x}} + \bar{\boldsymbol{\xi}}^1) \qquad \forall \bar{\boldsymbol{x}} \quad \text{on } \overline{\Sigma}. \tag{43}$$

To do so, we use a Taylor expansion at the order 1, which is valid since ϕ_∞ is defined on the whole domain Ω_∞:

$$\bar{\phi}^0_\infty(\bar{\boldsymbol{x}}) = \phi_\infty(\bar{\boldsymbol{x}}) \qquad \forall \bar{\boldsymbol{x}} \quad \text{on } \overline{\Sigma}, \tag{44a}$$

$$\bar{\phi}^1_\infty(\bar{\boldsymbol{x}}) = \boldsymbol{\nabla}\phi_\infty(\bar{\boldsymbol{x}}) \cdot \boldsymbol{\xi}^1 = \boldsymbol{u}_\infty \cdot \boldsymbol{\xi}^1 \qquad \forall \bar{\boldsymbol{x}} \quad \text{on } \overline{\Sigma}. \tag{44b}$$

The linear potential of the ambient flow perturbed by the vibrating solid can therefore be obtained from equations (42) and (44) as

$$\phi = \bar{\phi}^0_p + \bar{\phi}^1_p + \bar{\phi}^0_\infty + \bar{\phi}^1_\infty + \mathcal{O}\left(\varepsilon^2\right) \quad \text{on } \Sigma_{(t)}. \tag{45}$$

The velocity $\boldsymbol{u}$ at orders 0 and 1 is then calculated using the gradient and the potential from the reference configuration (see Appendix A for details on the calculation):

$$\bar{\boldsymbol{u}}^0 = \overline{\boldsymbol{\nabla}}\bar{\phi}^0 \quad \text{on } \overline{\Sigma}, \tag{46a}$$

$$\bar{\boldsymbol{u}}^1 = \overline{\boldsymbol{\nabla}}\bar{\phi}^1 - \left[\overline{\nabla}^{\mathrm{T}}\bar{\boldsymbol{\xi}}^1\right]\bar{\boldsymbol{u}}^0 \quad \text{on } \overline{\Sigma}. \tag{46b}$$

In a similar fashion, the pressure given by (34) can be split into order 0 and 1 terms. Knowing that for a constant ambient flow $\boldsymbol{u}_\infty$ the order 0 potential $\bar{\phi}^0$ does not vary with time (see equations (42a) and (44a)), one obtains:

$$\frac{\bar{p}^0}{\rho_f} = \Psi_\infty - \frac{1}{2}(\bar{\boldsymbol{u}}^0)^2 - g\boldsymbol{e}_z \cdot \bar{\boldsymbol{x}}, \tag{47a}$$

$$\frac{\bar{p}^1}{\rho_f} = \frac{\partial \bar{\boldsymbol{\xi}}^1}{\partial t} \cdot \bar{\boldsymbol{u}}^0 - \bar{\boldsymbol{u}}^1 \cdot \bar{\boldsymbol{u}}^0 - \frac{\mathrm{d}\bar{\phi}^1}{\mathrm{d}t} - g\boldsymbol{e}_z \cdot \bar{\boldsymbol{\xi}}^1. \tag{47b}$$

This enables to determine the virtual work on the fluid-structure interface (35) at both orders 0 and 1:

$$f^0_{ext} = \rho_f \int_{\bar{\Sigma}} \bar{p}^0 \bar{\boldsymbol{n}} \cdot \delta\boldsymbol{\xi} \,\mathrm{d}\bar{\Sigma} \tag{48a}$$

$$f^1_{ext} = \int_{\bar{\Sigma}} \left[\bar{p}^0 \bar{\boldsymbol{\tau}}^1 + \rho_f \left(\bar{\boldsymbol{u}}^0 \cdot \left(\frac{\partial \bar{\boldsymbol{\xi}}^1}{\partial t} - \bar{\boldsymbol{u}}^1 \right) - \frac{\mathrm{d}\bar{\phi}^1}{\mathrm{d}t} - g\bar{\boldsymbol{\xi}}^1 \cdot \boldsymbol{e}_z \right) \bar{\boldsymbol{n}} \right] \cdot \delta\boldsymbol{\xi} \,\mathrm{d}\bar{\Sigma}, \tag{48b}$$

It is convenient to decompose the order 0 pressure into ambient and perturbed contributions in order to isolate the different contributions of this work later (see below equation (59)):

$$\frac{\bar{p}^0_\infty}{\rho_f} = \Psi_\infty - \frac{1}{2}U^2_\infty - g\bar{\boldsymbol{x}} \cdot \boldsymbol{e}_z \tag{49a}$$

$$\frac{\bar{p}^0_p}{\rho_f} = -\frac{1}{2}(\bar{\boldsymbol{u}}^0_p)^2 - \bar{\boldsymbol{u}}^0_p \cdot \bar{\boldsymbol{u}}_\infty. \tag{49b}$$

The value of $\bar{\boldsymbol{u}}^1$ in the work expression (48) could be replaced by expression (46b). However, calculating the whole spatial gradient of a scalar field ϕ knowing only its value at the interface is inconvenient. Hence the necessity to redevelop the scalar product $\bar{\boldsymbol{u}}^0.\bar{\boldsymbol{u}}^1$ using equation (A.10) from Appendix A as well as equations (48) and (49) enables to use only the surface gradient of $\bar{\phi}$ instead of its complete gradient in the expression of the fluid forces perturbations:

$$f^1_{ext} = \int_{\bar{\Sigma}} \left[(\bar{p}^0_p + \bar{p}^0_\infty) \bar{\boldsymbol{\tau}}^1 + \rho_f \left(\bar{\boldsymbol{u}}^0 \cdot \left(\frac{\partial \bar{\boldsymbol{\xi}}^1}{\partial t} - \bar{\boldsymbol{\nabla}}_S \bar{\phi}^1 + \bar{\boldsymbol{\nabla}}^{\mathrm{T}}_S \bar{\boldsymbol{\xi}}^1 \bar{\boldsymbol{u}}^0 \right) - \frac{\mathrm{d}\bar{\phi}^1}{\mathrm{d}t} - g\bar{\boldsymbol{\xi}}^1 \cdot \boldsymbol{e}_z \right) \bar{\boldsymbol{n}} \right] \cdot \delta\boldsymbol{\xi} \,\mathrm{d}\bar{\Sigma}. \tag{50}$$

It is possible to use the above expression for numerical calculation of the fluid loads on the flexible structure. The work of the fluid above can be coupled with the structure dynamics through equation (1), which is the aim of the next section.

3. Numerical calculation of the fluid mass, gyroscopic and stiffness contributions

The structure characteristics K_s and M_s are supposed to be known, and this article does not focus on their calculation. Hence, in order to obtain the dynamical solution of equation (1) associated with the fluid linearized efforts exerted on the structure, an approximation of the solution is derived through a numerical procedure based on a triangular surface mesh of the fluid-structure interface. First, the potential of the fluid will be solved using the BEM. Based on this potential solution, the resulting load of the fluid will be determined using FEM operators, allowing us to couple the flow with the structure deformations. In order to find a numerical approximation of the potential for a steady ambient flow, we used the BEM based on the integral representation (42) which approximates the integral over the fluid-structure interface [21]. The interface is discretized into triangular elements connected to N_{DOF} nodes. The variables are interpolated using linear basis functions attached to the mesh nodes. According to the collocation method [21], the evaluation points $\boldsymbol{y}_i$ are also located on the mesh nodes. BEM operators $[G]_{n\times 3n}$, $[G']_{n\times 3n}$ (single layer operators) and $[H]_{n\times n}$, $[H']_{n\times 3n}$ (double layer operators) are introduced as:

$$\sum_j [G]_{ij} \{\bar{\boldsymbol{u}}\}_j \simeq \int_{\overline{\Sigma}} -\overline{\boldsymbol{G_n}}^0_{(\bar{\boldsymbol{x}},\bar{\boldsymbol{y}}_i)} \cdot \bar{\boldsymbol{u}}_{(\bar{\boldsymbol{x}})} \mathrm{d}\overline{\Sigma}_{(\bar{\boldsymbol{x}})}, \tag{51a}$$

$$\sum_j \left[G'_{(\boldsymbol{u}_\infty)}\right]_{ij} \{\bar{\boldsymbol{\xi}}\}_j \simeq \int_{\overline{\Sigma}} -\overline{\boldsymbol{G_n}}^1_{\left(\bar{\boldsymbol{x}},\bar{\boldsymbol{y}}_i,\bar{\boldsymbol{\xi}}\right)} \cdot \boldsymbol{u}_\infty \mathrm{d}\overline{\Sigma}_{(\bar{\boldsymbol{x}})}, \tag{51b}$$

$$\sum_j [H]_{ij} \{\bar{\phi}\}_j \simeq \{\bar{\phi}\}_i - \int_{\overline{\Sigma}} \overline{\partial_n G}^0_{(\bar{\boldsymbol{x}},\bar{\boldsymbol{y}}_i)} \left(\bar{\phi}_{(\bar{\boldsymbol{x}})} - \bar{\phi}_{(\bar{\boldsymbol{y}}_i)}\right) \mathrm{d}\overline{\Sigma}_{(\bar{\boldsymbol{x}})}, \tag{51c}$$

$$\sum_j \left[H'_{(\bar{\phi})}\right]_{ij} \{\bar{\boldsymbol{\xi}}\}_j \simeq \int_{\overline{\Sigma}} \overline{\partial_n G}^1_{\left(\bar{\boldsymbol{x}},\bar{\boldsymbol{y}}_i,\bar{\boldsymbol{\xi}}\right)} \left(\bar{\phi}_{(\bar{\boldsymbol{x}})} - \bar{\phi}_{(\bar{\boldsymbol{y}}_i)}\right) \mathrm{d}\overline{\Sigma}_{(\bar{\boldsymbol{x}})}. \tag{51d}$$

The brackets $[\bullet]$ denote matrices and $\{\bullet\}$ denote vectors whose j^{th} component is the value of the variable at the node $\bar{\boldsymbol{y}}_j$. The reader might refer to Appendix A for the expressions of $\overline{\boldsymbol{G_n}}^0$,$\overline{\boldsymbol{G_n}}^1$,$\overline{\partial_n G}^0$ and $\overline{\partial_n G}^1$. The collocation method consists in determining each row i of the BEM operators by associating it to a reference point $\bar{\boldsymbol{y}}_i$. The integration is then calculated using Gaussian weights, the value of $\bar{\boldsymbol{x}}$ and $\bar{\phi}(\bar{\boldsymbol{x}})$ being obtained at each Gauss point from their values at the element nodes using a linear interpolation. The finer the mesh, the better the discrete expression (51) approximates their continuous counterparts. However, when $\bar{\boldsymbol{x}}$ is located in the same triangle as $\bar{\boldsymbol{y}}_i$, the norm $\|\boldsymbol{x} - \boldsymbol{y}_i\|$ is nil at $\bar{\boldsymbol{x}} = \bar{\boldsymbol{y}}_i$, which means the integral over the triangle is improper and its value has to be calculated carefully. For the double layer term

$$\overline{\partial_n G}^0 = \frac{(\bar{\boldsymbol{x}} - \bar{\boldsymbol{y}}_i).\bar{\boldsymbol{n}}}{\|\bar{\boldsymbol{x}} - \bar{\boldsymbol{y}}_i\|^3},$$

the planar shape of the triangles implies that any vector connecting two points of a same triangle is included in the triangle, and is consequently perpendicular to the triangle normal, hence:

$$(\bar{\boldsymbol{x}} - \bar{\boldsymbol{y}}_i).\bar{\boldsymbol{n}} = 0 \quad \forall \bar{\boldsymbol{x}}, \bar{\boldsymbol{y}}_i \text{ in the same triangle.} \tag{52}$$

Consequently, the term $\overline{\partial_n G}^0$ is trivial to integrate in that case. Though equation (52) simplifies the implementation of the BEM by preventing the calculation of highly singular terms, [32] mentions that this triangle mesh approximation causes a discretization error of the order of $\delta\kappa/4\pi$, where δ is the perimeter of the triangle and κ the mean curvature of the real surface $\overline{\Sigma}$. As shown in equation (A.3d), the double layer linearized term is strongly singular for $\bar{\boldsymbol{x}} \to \bar{\boldsymbol{y}}$, and, as a consequence, one might expect that difficulties could arise integrating it. However, for the same reason that the scalar product $(\bar{\boldsymbol{x}} - \bar{\boldsymbol{y}}) \cdot \bar{\boldsymbol{n}}$ is nil at order zero, the term $\overline{\partial_n G}^1$ will vanish when $\bar{\boldsymbol{x}}$ and $\bar{\boldsymbol{y}}$ are in the same triangle: the rotated normal associated with the deformed triangle will remain perpendicular to the deformed vector $\bar{\boldsymbol{x}} + \bar{\boldsymbol{\xi}}^1(\bar{\boldsymbol{x}}) - (\bar{\boldsymbol{y}} + \bar{\boldsymbol{\xi}}^1(\bar{\boldsymbol{y}}))$. This ensures that the double layer term at order one $\overline{\partial_n G}^1$ vanishes too when both $\bar{\boldsymbol{x}}$ and $\bar{\boldsymbol{y}}$ are on the same triangle. On the contrary, the term $\overline{\boldsymbol{G_n}}^0$ does not cancel for $\bar{\boldsymbol{x}} \to \bar{\boldsymbol{y}}_i$ and the integral has to be calculated carefully. In this article, their implementation was done using a Lachat-Watson transformation as detailed in [33]. Similarly, the term $\overline{\boldsymbol{G_n}}^1$ has to be calculated carefully. Its singularity for $\bar{\boldsymbol{x}} \to \bar{\boldsymbol{y}}$ is of the same order than $\overline{\boldsymbol{G_n}}^0$: more particularly, one might notice how the term $(\bar{\boldsymbol{x}} - \bar{\boldsymbol{y}}).(\bar{\boldsymbol{\xi}}^1(\bar{\boldsymbol{x}}) - \bar{\boldsymbol{\xi}}^1(\bar{\boldsymbol{y}}) / \|\bar{\boldsymbol{x}} - \bar{\boldsymbol{y}}\|$ in $\overline{\boldsymbol{G_n}}^1$ is in $\mathcal{O}\left(\|\bar{\boldsymbol{x}} - \bar{\boldsymbol{y}}\|\right)$ since $\bar{\boldsymbol{\xi}}^1(\bar{\boldsymbol{x}}) - \bar{\boldsymbol{\xi}}^1(\bar{\boldsymbol{y}})$ is linear when $\bar{\boldsymbol{x}}$ and $\bar{\boldsymbol{y}}$ are in the same triangle, just like the term $\|\bar{\boldsymbol{x}} - \bar{\boldsymbol{y}}\|$ for $\overline{\boldsymbol{G_n}}^0$. As a consequence, the term $\overline{\boldsymbol{G_n}}^1$ has been implemented using the Lachat-Watson transformation, similarly to $\overline{\boldsymbol{G_n}}^0$.

Another difficulty with this approach is that the BEM operators are full. As a consequence, their storage cost is in $\mathcal{O}\left(N_{DOF}^2\right)$. The latter could be reduced by using one of the BEM acceleration methods. As explained by [41], the Hierarchical matrix method would be best suited here as it allows to calculate multiple matrix-vector products based on a single compressed matrix calculations, on the contrary to the Fast Multipole Method which would require to calculate a new approximation from scratch for each matrix-vector product.

The implementation of an accelerated BEM is however not in the scope of this article. Let us remark that, in order to reduce the required memory when computation is implemented, both linearized operators can be calculated as one:

$$[J] = [G'] + \left[H'_{(\bar{\phi}_p^0)}\right] . \tag{53}$$

Thanks to the linearization, BEM operators are calculated only once, at the cost of storing three matrix operators instead of two, enabling to take into account the variations associated with any small mesh deformation without recalculating the discretized BEM operators as done in previous studies on fluid-structure interaction such as [9, 10, 11, 12, 13]. From equation (42), the order 0 and 1 solutions of the potential can therefore be obtained by inverting the linear systems with a GMRes algorithm:

$$[H]\left\{\bar{\phi}_p^0\right\} = [G]\left\{-\boldsymbol{u}_\infty\right\}, \tag{54a}$$

$$[H]\left\{\bar{\phi}_p^1\right\} = [J]\left\{\bar{\boldsymbol{\xi}}^1\right\} + [G]\left\{\frac{\partial \bar{\boldsymbol{\xi}}^1}{\partial t}\right\}. \tag{54b}$$

Because the expression of $[J]$ depends on the field $\bar{\phi}_p^0$, this operator has to be computed once the order 0 system has been solved. The linear operators $[A]$, $[B]$ and $[U_\infty]$ are introduced as well:

$$[A] = [H]^{-1}[G], \tag{55a}$$

$$[B] = [H]^{-1}[J] + [U_\infty] \text{ with } [U_\infty]\{\bar{\boldsymbol{\xi}}\} = \{\boldsymbol{u}_\infty . \bar{\boldsymbol{\xi}}\} \tag{55b}$$

By combining (54) and (55), the linear calculation of the potential approximation at mesh nodes writes for an homogeneous ambient flow:

$$\left\{\phi^0\right\} = \left\{\phi_p^0\right\} + \left\{\phi_\infty^0\right\} = [A]\left\{-\boldsymbol{u}_\infty\right\} + [U_\infty]\{\bar{\boldsymbol{x}}\}, \tag{56a}$$

$$\left\{\phi^1\right\} = \left\{\phi_p^1\right\} + \left\{\phi_\infty^1\right\} = [A]\left\{\frac{\partial \bar{\boldsymbol{\xi}}^1}{\partial t}\right\} + [B]\left\{\bar{\boldsymbol{\xi}}^1\right\}. \tag{56b}$$

The present approach is similar to the panel method because it is based on the same integral representation of the solution of Laplace's equation. The main difference is in the way the associated integral equation is solved: we have adopted a direct resolution by looking for a polynomial field ϕ_p (linear in practice) whose values at the nodes are the unknowns of the problem (Boundary Element Method), whereas the panel method looks for ϕ_p in the form of a superposition of particular solutions associated with monopoles (source/well) or dipoles (doublet/vortex) whose intensities are the unknowns of the problem [34]. The advantage of the present approach is that one can obtain the dependence of the velocity potential solution on the movements and deformations of the immersed structure by directly differentiating the BEM operators with respect to a displacement variable of the interface. However, in the current implementation, the presence of the singularity of the solution at the wake has been omitted for simplification purposes, which does not allow imposing a Kutta condition at the trailing edge of the fins, in order to take into account the circulation effects around the body. As a consequence, the obtained solution does not allow to represent the phenomena of lift and pressure drag [34]. However, when considering the hull without fins, the pressure fluctuations seem to be relatively close to more complete RANS type simulations as shown in Figure 5, which gives confidence in the results of such a method in finless configurations. Concerning the fins, a simple aerodynamic model might be added as done by [6], or the present approach might be extended to take into account vortex sheets drawing inspiration from [3, 8, 28] as mentioned in the conclusion of this article.
Using equations (56), we can now compute the potential solution of the fluid at orders 0 and 1, and an approximation of the dynamical fluid forcing for an homogeneous stationary ambient flow from equation (50) can be computed using FEM operators. In order to do so, the following FEM bilinear operators are introduced:

$$
\begin{aligned}
\{\delta\boldsymbol{\xi}\}^{\mathrm{T}}\,[C]\,\{p\} &\simeq \int_{\overline{\Sigma}} \bar{p}\bar{\boldsymbol{n}}\cdot\delta\boldsymbol{\xi}\,\mathrm{d}\overline{\Sigma},\\
\{\delta\boldsymbol{\xi}\}^{\mathrm{T}}\left[D_{(\bar{\boldsymbol{u}}^0)}\right]\{\phi\} &\simeq \int_{\overline{\Sigma}} \bar{\boldsymbol{u}}^0\cdot\overline{\boldsymbol{\nabla}}_S\bar{\phi}\quad \bar{\boldsymbol{n}}\cdot\delta\boldsymbol{\xi}\,\mathrm{d}\overline{\Sigma},\\
\{\delta\boldsymbol{\xi}\}^{\mathrm{T}}\left[E_{(\bar{\boldsymbol{u}}^0,\bar{\boldsymbol{u}}^0)}\right]\{\bar{\boldsymbol{\xi}}\} &\simeq \int_{\overline{\Sigma}} -\bar{\boldsymbol{u}}^0\cdot\left(\left[\overline{\nabla}_S^T\bar{\boldsymbol{\xi}}\right]\bar{\boldsymbol{u}}^0\right)\quad \bar{\boldsymbol{n}}\cdot\delta\boldsymbol{\xi}\,\mathrm{d}\overline{\Sigma},\\
\{\delta\boldsymbol{\xi}\}^{\mathrm{T}}\left[F_{(\bar{\boldsymbol{u}}^0)}\right]\{\bar{\boldsymbol{\xi}}\} &\simeq \int_{\overline{\Sigma}} -\bar{\boldsymbol{\xi}}\cdot\bar{\boldsymbol{u}}^0\quad \bar{\boldsymbol{n}}\cdot\delta\boldsymbol{\xi}\,\mathrm{d}\overline{\Sigma},\\
\{\delta\boldsymbol{\xi}\}^{\mathrm{T}}\left[L_{\left(\bar{p}_p^0\right)}\right]\{\bar{\boldsymbol{\xi}}\} &\simeq \int_{\overline{\Sigma}} -\bar{p}_p^0\,\bar{\boldsymbol{\tau}}^1_{(\bar{\boldsymbol{\xi}})}\cdot\delta\boldsymbol{\xi}\,\mathrm{d}\overline{\Sigma},\\
\{\delta\boldsymbol{\xi}\}^{\mathrm{T}}\,[K_s]\,\{\bar{\boldsymbol{\xi}}\} &\simeq K_s(\bar{\boldsymbol{\xi}},\delta\boldsymbol{\xi}),\\
\{\delta\boldsymbol{\xi}\}^{\mathrm{T}}\,[M_s]\left\{\frac{\partial^2\bar{\boldsymbol{\xi}}}{\partial t^2}\right\} &\simeq M_s\left(\frac{\partial^2\bar{\boldsymbol{\xi}}}{\partial t^2},\delta\boldsymbol{\xi}\right).
\end{aligned}
\tag{57}
$$

The operators $[D]$, $[E]$, $[F]$ and $[G]$ are functions of the order 0 solutions $\bar{\boldsymbol{u}}^0$ and $\bar{p}^0$. Therefore, they should be recalculated when the stationary state changes. The operators K_s and M_s were introduced in equation (1): we consider here their FEM discretized counterparts $[K_s]$ and $[M_s]$. The dynamical equation of the fluid-structure coupled system (1) becomes:

$$
\begin{aligned}
&\left([M_s]+\rho_f\,[C]\,[A]\right)\left\{\frac{\partial^2\bar{\boldsymbol{\xi}}}{\partial t^2}\right\}+\rho_f\left([C]\,[B]+\left[D_{(\bar{\boldsymbol{u}}^0)}\right][A]+\left[F_{(\bar{\boldsymbol{u}}^0)}\right]\right)\left\{\frac{\partial\bar{\boldsymbol{\xi}}}{\partial t}\right\}+\dots\\
&\left([K_s]+\rho_f\Big[\left[D_{(\bar{\boldsymbol{u}}^0)}\right][B]+\left[E_{(\bar{\boldsymbol{u}}^0,\bar{\boldsymbol{u}}^0)}\right]+\left[L_{(\bar{p}_p)}\right]+\left[L_{(\bar{p}_\infty)}\right]+\left[F_{(-g\boldsymbol{e}_z)}\right]\Big]\right)\{\bar{\boldsymbol{\xi}}\}=0.
\end{aligned}
\tag{58}
$$

One can identify from the above equation the mass $[M_f]$, gyroscopic $[G_f]$ and stiffness $[K_f]$ matrices induced by the coupling with the flow:

$$[M_f]=\rho_f\,[C]\,[A]\,, \tag{59a}$$

$$[G_f]=\rho_f\left([C]\,[B]+\left[D_{(\bar{\boldsymbol{u}}^0)}\right][A]+\left[F_{(\bar{\boldsymbol{u}}^0)}\right]\right), \tag{59b}$$

$$[K_f]=\rho_f\left(\left[D_{(\bar{\boldsymbol{u}}^0)}\right][B]+\left[E_{(\bar{\boldsymbol{u}}^0,\bar{\boldsymbol{u}}^0)}\right]+\left[L_{\left(\bar{p}_p^0\right)}\right]+\left[L_{(\bar{p}_\infty)}\right]+\left[F_{(-g\boldsymbol{e}_z)}\right]\right). \tag{59c}$$

It is important to note that the term "gyroscopic" used in this article and taken from [29] refers here to fluid forces that are conservative and linear with the velocity of the structure (as mentioned below), not to be confused with the torque associated with the rotation of a solid. By linearity of the operators in the above equation, and noticing also that $\bar{\boldsymbol{u}}^0$ is linear with respect to $\boldsymbol{u}_\infty$, one can show that the stiffness operator $\left([K_f]-\left[N_{(\bar{p}_\infty)}\right]\right)$ is quadratic to the ambient flow velocity $\boldsymbol{u}_\infty$, the gyroscopic operator $[G_f]$ is linear with $\boldsymbol{u}_\infty$, whereas the added mass operator $[M_f]$ does not vary upon $\boldsymbol{u}_\infty$, which is coherent wit [6]. This is the reason why the operator $[M_f]$ is often calculated in the case of a fluid at rest, even though it is used in the dynamical equation with a flowing fluid, as in reference [6]. In their study [6], Li showed using the Lagrange equations that the added mass and stiffness operators associated with elastic movements are symmetric while the gyroscopic operator is skew-symmetric. It is important to note that these properties are verified only with the irrotational flow hypotheses usually used for bluff bodies and are not valid for slender bodies such as wings which induce vorticity in the flow. According to Ziegler [29], such properties of the operators are expected for conservative systems, which is the case of the fluid: an incompressible, ideal, irrotational flow does not lose energy and does not transfer energy to infinity either. With a Newtonian approach, these (skew-)symmetry attributes do not appear as naturally as with the Lagrange equations, but [35] has shown the symmetry properties of the added mass operator with the former approach. It is possible as well to implement the BEM method based on a variational formulation of the integral representation [35]: this approach would ensure the symmetry of the added mass matrix at the expense of more integrations. For

this reason, the collocation method used to implement the BEM in this article seems to be an acceptable compromise between accuracy and numerical effort. However, the (skew-)symmetry of the fluid operators has been numerically evaluated in section 4.
Finally, the fluid-structure dynamical equation becomes

$$([M_s] + [M_f]) \left\{ \frac{\partial^2 \bar{\boldsymbol{\xi}}}{\partial t^2} \right\} + [G_f] \left\{ \frac{\partial \bar{\boldsymbol{\xi}}}{\partial t} \right\} + ([K_s] + [K_f]) \left\{ \bar{\boldsymbol{\xi}} \right\} = 0. \tag{60}$$

Equation (60) is a monolithic equation: because the fluid and the structure dynamics are contained in a unique equation, it allows solving both simultaneously, contrary to partitioned approaches which require an alternating resolution of the fluid and structure equations. Moreover, this monolithic equation has the advantage of not depending explicitly on the fluid variables, since they have been eliminated in favor of their expressions in $\boldsymbol{\xi}$ and its time derivatives. It is of particular interest to determine the appearance of instabilities of the structure, as well as a better prediction of the structure behavior [6]. According to Ziegler's classification [29, 30], if the loads associated with the stiffness K_s of the structure are conservative (or equivalently if K_s is symmetric), then the system described by (60) is a gyroscopic conservative linear system, as it contains non-circulatory loads (as K_s, K_f and M_f are symmetric) and gyroscopic loads (as G_f is skew-symmetric). Such systems present a risk of losing stability whenever the associated non-circulatory forces become non-positive (which might be caused only by the non-positiveness of K_f since M_f is necessarily positive), although in some cases the gyroscropic loads G_f are capable of preventing such instabilities [29]. More specifically post-divergence flutter by coupling of two divergent modes can also occur in such systems according to Paidoussis [30]. However, common unstable aeroelastic phenomena such as flutter by frequency crossing or wake flutter, caused respectively by the unsymmetry of the stiffness operator and the non-positiveness of the damping operator [31, 25] are not predicted by this equation, but could arise for instance with the addition of circulatory effects around the fins. The next section aims to quantify the errors in the fluid loads from equation (60) associated with the numerical approximation and with the order 1 approximation.

4. Quantification of the error from numerical and linear approximations

In order to quantify the error of the fluid operators associated with the fluid-structure characterization exhibited in equation (60), this section focuses on four test cases.

- With a view to validating the BEM procedure, the quasi-steady solution of a homogeneous longitudinal ambient flow past a revolution ellipsoid is studied, comparing the velocity potential analytic solution with the BEM approximation.
- The potential flow model solved with the BEM is compared with more accurate fluid simulation based on RANS in a second test-case, enabling to see the regions where the potential flow model cannot capture all the physics, but to validate as well the overall good capture of the pressure fluctuations over the interface by the BEM.
- The third test case compares the linear approximation introduced in sections 2 and 3 with a numerical non-linear solution, studying the associated error on the fluid stiffness operator in the case of elastic movements, depending on a small parameter ε.
- Finally, the fourth test case quantifies the numerical error on the fluid mass and gyroscopic operators in the case of rigid body movements of the structure, enabling to validate the FEM approach and to assess the convergence of the mixed FEM-BEM approach introduced in this document.

4.1. BEM approximation

In order to validate the implementation of the BEM procedure at order zero, a simple test case is presented below. It consists of a revolution ellipsoid (also referred to as a spheroid). Its semi axis are of length L (for *length*) and D (for *diameter*) respectively. Its aspect ratio $\mathcal{S}$ is defined as

$$\mathcal{S} = \frac{L}{D}. \tag{61}$$

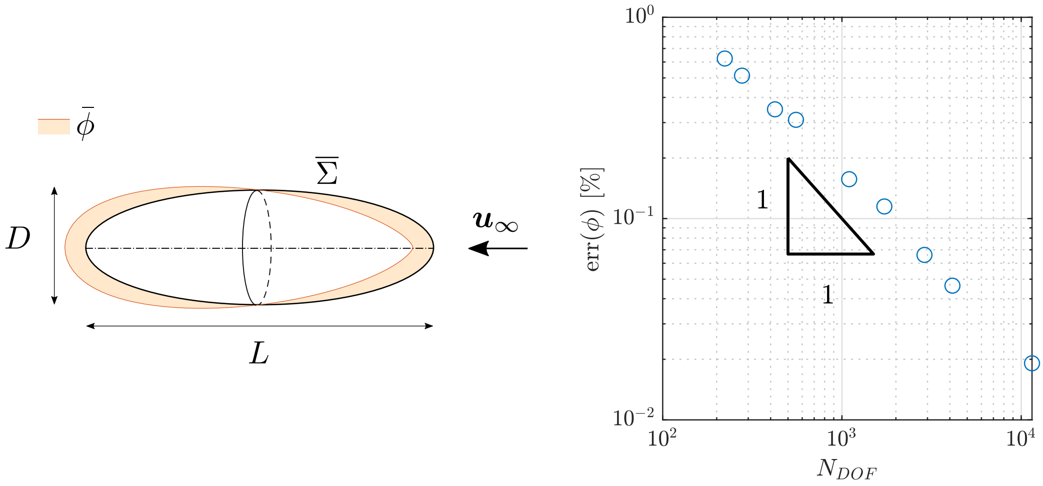

Figure 3: Left: Side view of a spheroid of aspect ratio $\mathcal{S} = 3$, with the potential solution $\bar{\phi}$ associated with a longitudinal ambient flow. Right: relative error of the numerical solution $\left\{\bar{\phi}_{\mathrm{BEM}}\right\}$ compared to its theoretical value as a function of the number of nodes. The triangle enables visualizing the $\mathcal{O}\left(N_{DOF}^{-1}\right)$ slope.

For this test case, an aspect ratio of $\mathcal{S} = 3$ is used. The ambient flow has a uniform longitudinal direction of amplitude U_∞. An analytic expression of the resulting potential at the interface can be obtained from [36], leading to the following expression:

$$\bar{\phi}(\bar{\boldsymbol{x}}) = U_\infty \bar{\boldsymbol{x}}.\boldsymbol{e}_x f(\mathcal{S}), \quad \bar{\boldsymbol{x}} \in \overline{\Sigma}, \tag{62}$$

where f is a dimensionless analytic function of the aspect ratio (see figure 3 left for an outview).
In order to validate the quasi-steady BEM procedure, the analytic potential solution is compared to numerical results. The discrete vector $\left\{\bar{\phi}_{\mathrm{BEM}}\right\}$ has been obtained with the BEM for various mesh refinements in order to study the convergence of the method. The numerical results are presented in figure 3, where the error has been defined relatively to the exact solution $\bar{\phi}$ and is defined with the $L^2(\overline{\Sigma})$ error:

$$\mathrm{err}\left(\bar{\phi}^*_{\mathrm{BEM}}\right) = \frac{\left\|\bar{\phi}^*_{\mathrm{BEM}} - \bar{\phi}^*\right\|_{L^2(\overline{\Sigma})}}{\left\|\bar{\phi}^*\right\|_{L^2(\overline{\Sigma})}} \text{ with } \|a\|_{L^2(\overline{\Sigma})} = \sqrt{\int_{\overline{\Sigma}} a(\bar{\boldsymbol{x}})^2 \mathrm{d}\overline{\Sigma}}. \tag{63}$$

The integral over $\overline{\Sigma}$ in the above equation is approximated using the values at the nodes and the FEM. As shown in Figure 3, the BEM converges toward the analytic solution in $\mathcal{O}\left(N_{DOF}^{-1}\right)$.

4.2. Comparison of RANS method and BEM

In order to further verify if the results obtained for a potential flow solved with the BEM enable to capture well the fluid forces around an interface, this section compares results of the quasi-steady order zero pressure repartition solved using the BEM with results obtained with a RANS simulation, which allows to take into account the effects of turbulence unlike the potential flow model the BEM is based on. The RANS simulations are based on a Spalart-Allmaras turbulence model, and are obtained for a compressible flow at $\mathcal{R}_e = 2.2 \times 10^6$ using the code elsA from ONERA. The comparison of the dynamic pressure repartition between the BEM and the RANS method is presented in Figure 5 on a vertical slice $y = 0$ of the interface including both the symmetry axis of the structure and the velocity vector of the ambient flow $\boldsymbol{u}_\infty$. Because the static pressure is straightforward to obtain, its value has been removed in order to compare only the dynamic pressure $p_{dyn} = -\frac{1}{2}\boldsymbol{u}^2$. which is more challenging to predict. One can see that the BEM and RANS pressure repartition are similar almost everywhere on the interface slice presented here, except for two areas.

First, on the top rear of the interface, the BEM dynamic pressure is overestimated (reminding that with the projection of p_{dyn} in Figure 5, a curve closer to the interface means a higher pressure). This means that the pressure predicted by the RANS will create a suction force on the top of the interface which is not captured by the BEM. It is due to the fact that, because of the angle of attack, the flow around the interface creates a lift toward $z > 0$. Because of the d'Alembert paradox, the potential model used for the BEM cannot predict any lift on the structure as mentioned by [1], hence this first divergence between the two methods. The second difference between these methods is that the BEM predicts a stationary point at the rear of the structure (a nil dynamic pressure associated with a nil velocity), whereas the RANS calculation does not predict a stationary point because of turbulence causing the fluid to stall locally at the rear of the structure. As turbulence is not taken into account with the potential flow hypothesis, BEM is not able to predict the stall phenomenon. Let us remark that the fluctuation spikes of pressure that appear on the blue curves apart from the symmetry axis ($[x, z] \simeq \{[-20, 5], [-15, -3], [16, 1], [16, -1]\}$ are only visualization artifacts due to the linear interpolation of the pressure field between different mesh zones, and since the RANS mesh is singular on the symmetry axis of the mesh, the fluid perceives the front and rear of the interface as a hole very locally, hence the pressure local spikes of the RANS results at an altitude $z = 0$. Further comparisons between potential flow theory and experimental measurements can be found in [38], where the pressure repartition around a non-axisymetric ellipsoid of aspect ratio $\mathcal{S} = 3.5$ obtained with an analytic potential method is compared with both RANS simulations and experimental measurements at $\mathcal{R}_e = \mathcal{O}\left(10^6\right)$. This study leads to similar conclusions: the potential pressure repartition compares well except for the rear of the body where stall occurs.

The results presented in this section confirms statements that had been made in the literature [1]: at sufficiently low angles of attack, the potential flow hypothesis enables to predict the pressure fluctuations of the flow, even thought it cannot capture the lift caused by the circulation induced on the flow in practice, and it is not able to predict turbulent effects at the rear of the body. Moreover, as the RANS simulations are associated with a compressible fluid, these results tend to validate the hypothesis that the compressibility of the fluid plays a negligible role at the scale of airships.

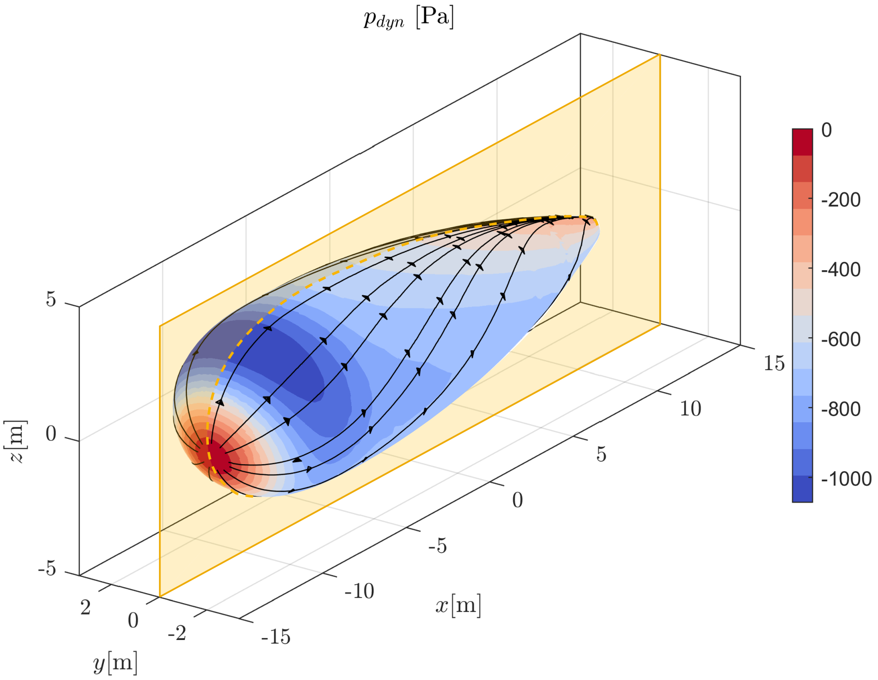

Figure 4: Dynamic pressure repartition around a generic airship shape with a symmetry axis. The orange slice is the plane $y = 0$ used to plot the pressure in Figure 5. The ambient flow has an angle of attack of 10^o and an amplitude of 34 m/s (see Figure 5 for a visualization of the ambient flow).

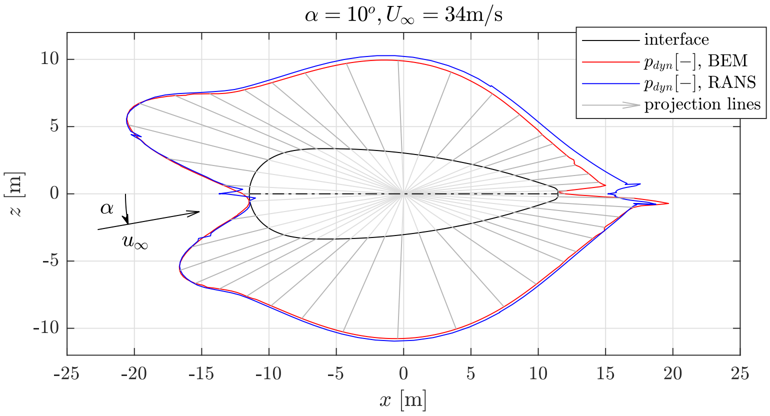

Figure 5: Comparison of the dynamic pressure associated with the steady ambient flow on a generic airship shape shown in Figure 4. The ambient flow has an angle of attack of 10^o. The pressure amplitude is projected in a radial direction represented by the light grey lines. When the pressure curve is coincident with the interface, it signifies that there is no dynamic pressure at this point. If the pressure curve is outside the airship domain, it signifies that the dynamic pressure is negative. The BEM is calculated on a $N_{DOF} = 5713$ surface mesh. The RANS method was obtained for a compressible flow with a Spalart-Allmaras turbulence model at $\mathcal{R}_e = 2, 2.10^6$. For visualization purposes, the pressure which is supposed to be constant over the elements has been interpolated linearly for both methods, hence the relative smoothness of both curves.

4.3. First order approximation

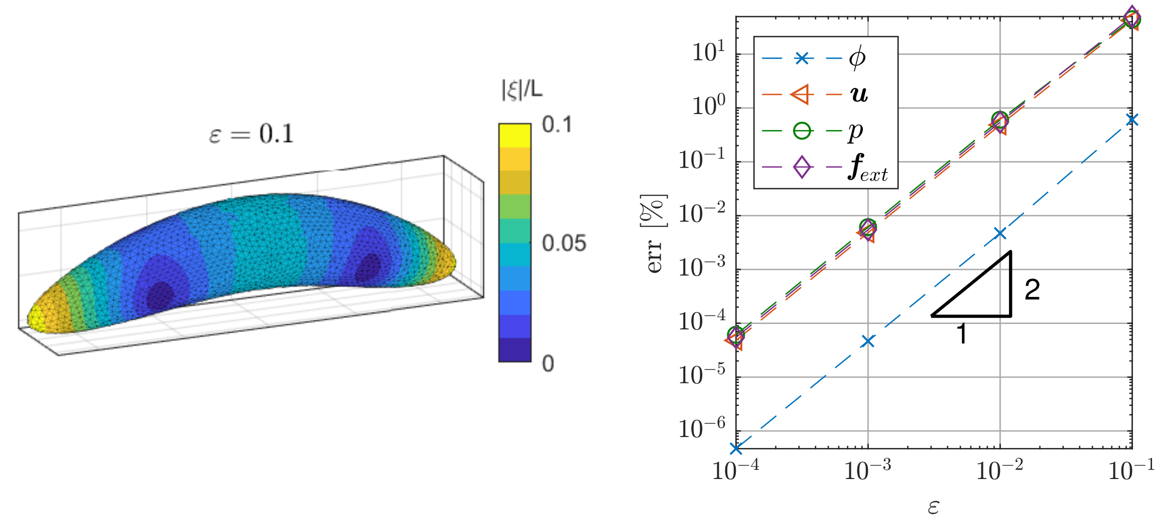

Figure 6: Left: shape of the deformed ellipsoidal fluid-structure interface for $\varepsilon = 0.1$. Right: evolution of the error in % associated with the linear prediction of the potential ϕ, the velocity $\boldsymbol{u}$, the pressure p and the force $\boldsymbol{f}_{ext}$ for a displacement $\boldsymbol{\xi}$ (as plotted on the left), as a function of ε. The triangle highlights the slope in $\mathcal{O}\left(\varepsilon^2\right)$ of the error.

In order to quantify the error associated with the linear approximation of fluid forces, the test case below compares both linear and non-linear fluid solutions with quasi-static approximation. The terms proportional to displacement $\bar{\boldsymbol{\xi}}$ in equations (54) and (60) are referred to as quasi-static: they correspond to the solution found when deformations occur at a negligible velocity and acceleration. In order to see to which extent the associated linearized fluctuations are valid or not, the results of the order 1 solution are compared with the variations of the non-linear solution obtained by physically deforming the mesh, hence using a finite difference method by calculating new BEM operators from scratch between consecutive mesh positions. Effects of gravity are not taken into account for this test case. The generalized fluid forces $\boldsymbol{f}_{ext}$ are introduced as:

$$\boldsymbol{f}_{ext} = -\left[M_f\right]\left\{\frac{\partial^2 \bar{\boldsymbol{\xi}}}{\partial t^2}\right\} - \left[G_f\right]\left\{\frac{\partial \bar{\boldsymbol{\xi}}}{\partial t}\right\} - \left[K_f\right]\left\{\bar{\boldsymbol{\xi}}\right\}. \tag{64a}$$

In order to validate the stiffness operator $[K_f]$, one can compare the linear predictions of ϕ, p, $\boldsymbol{f}_{ext}$ and $\boldsymbol{u}$ (see Appendix A for the detailed calculation of $\boldsymbol{u}$) with their non-linear counterpart. The linear prediction for those four variables are obtained for an arbitrary displacement $\boldsymbol{\xi}$ forming a banana shape (see Figure 6) representing the lowest frequency flexible modes of airship deformations according to [6]. More details about this displacement mode are given in section 5. The errors on ϕ, $\boldsymbol{u}$, p and $\boldsymbol{f}_{ext}$ are defined as:

$$\mathrm{err}(a) = \frac{\max\left(\left\|\bar{a}^0(\bar{\boldsymbol{x}}) + \bar{a}^1(\bar{\boldsymbol{x}}, \bar{\boldsymbol{\xi}}^1) - a(\bar{\boldsymbol{x}} + \bar{\boldsymbol{\xi}}^1)\right\|\right)}{\max\left(\left\|\bar{a}^0(\bar{\boldsymbol{x}})\right\|\right)}, \tag{65}$$

and are displayed in Figure 6. If the error is related to a scalar, the norm $\|\bullet\|$ in the equation above consists of the absolute value of its argument, if it is a vector, the euclidean norm is used. Figure 6 shows that the order 1 prediction of the fluid variables all tend to their respective non-linear value when $\varepsilon \to 0$, with an error in $\mathcal{O}\left(\varepsilon^2\right)$. This is in agreement with the fact that only terms of order 2 or more have been neglected. Furthermore, this test case validates the numerical implementation of the stiffness operator $[K_f]$ and quantifies the error associated with the linearization. In a similar way, it is expected that the error prediction of the added mass and gyroscopic loads from the fluid scale as $\mathcal{O}\left(\varepsilon^2\right)$, which will be verified in the next section.

4.4. Numerical approximation

In order to quantify the error associated with the numerical approximation of section 3, the fluid numerical operators are compared with analytical values found in the literature. This analytic reference comes from the non-linear fluid equations of a structure with rigid body movements in a perfect fluid with no gravity effects [37]. We present a linearization of these equations in Appendix A. Using this linearization as an analytic reference, the fluid operators obtained numerically with our method from equation (59) are compared with those obtained from the linearized fluid equation from Thomasson [37]. For a prolate ellipsoid of aspect ratio 5:1 (major axis length over minor axis length), the analytic value of $[M_f^{\mathrm{rig}}]^{ref}$ can be found in [39] (only the non nil coefficients are displayed below, with three significant digits):

$$[M_f^{\mathrm{rig}}]_{11}^{ref} = \frac{0.0591}{150}\pi\rho_f L^3 \tag{66a}$$

$$[M_f^{\mathrm{rig}}]_{22}^{ref} = [M_f^{\mathrm{rig}}]_{33}^{ref} = \frac{0.894}{150}\pi\rho_f L^3 \tag{66b}$$

$$[M_f^{\mathrm{rig}}]_{55}^{ref} = [M_f^{\mathrm{rig}}]_{66}^{ref} = \frac{0.700}{150}\frac{13}{250}\pi\rho_f L^5, \tag{66c}$$

The superscript $[\bullet]^{ref}$ stands for the terms obtained analytically. One can deduce the values of the rigid body gyroscopic operator $[G_f^{\mathrm{rig}}]^{ref}$ from the rigid body added mass operator (see Appendix A). Its non nil coefficients for an ambient flow $\boldsymbol{u}_\infty$ with an angle of attack $\pi/6$ relatively to the axis of revolution of the ellipsoid are:

$$[G_f^{\mathrm{rig}}]_{15}^{ref} = -[G_f^{\mathrm{rig}}]_{51}^{ref} = -0.350\rho_f L^2 U_\infty \tag{67a}$$

$$[G_f^{\mathrm{rig}}]_{26}^{ref} = [G_f^{\mathrm{rig}}]_{53}^{ref} = -[G_f^{\mathrm{rig}}]_{62}^{ref} = -[G_f^{\mathrm{rig}}]_{35}^{ref} = 0.606\rho_f L^2 U_\infty. \tag{67b}$$

Since the stiffness operator has already been validated in the case of an elastic deformation in the previous section, we do not consider this operator in this section. The fluid operators from equation (59) can be projected on the rigid body movements of the structure to be compared with the operators $[M_f^{\mathrm{rig}}]^{ref}$ and $[D_f^{\mathrm{rig}}]^{ref}$. These rigid body movements can be described with the displacement $\boldsymbol{d}$ of the structure's center of volume and the rotation $\boldsymbol{\theta}$, which relate to the structure displacements with the operator $\mathbb{Q}$:

$$\bar{\boldsymbol{\xi}}^1 = \mathbb{Q}\begin{pmatrix} \bar{\boldsymbol{d}}^1 \\ \bar{\boldsymbol{\theta}}^1 \end{pmatrix}, \tag{68a}$$

$$\mathbb{Q} = [\mathbb{1}, -\bar{\boldsymbol{x}}_\times]. \tag{68b}$$

The reduced fluid operators on rigid body modes are computed as:

$$[M_f]^{num} = \mathbb{Q}^{\mathrm{T}}[M_f]\mathbb{Q}, \quad [G_f]^{num} = \mathbb{Q}^{\mathrm{T}}[M_f]\mathbb{Q}. \tag{69}$$

The superscript $[\bullet]^{num}$ stands for the terms obtained numerically. The comparison between the analytic operators displayed in equations (66) and (67) with our model, for meshes with a varying number of nodes N_{DOF}, gives a relative error displayed in Figure 7, calculated with respect to the Frobenius norm:

$$\mathrm{err}([\bullet]) = \frac{\left\|[\bullet]^{num} - [\bullet]^{ref}\right\|_{\mathrm{fro}}}{\left\|[\bullet]^{ref}\right\|_{\mathrm{fro}}}. \tag{70}$$

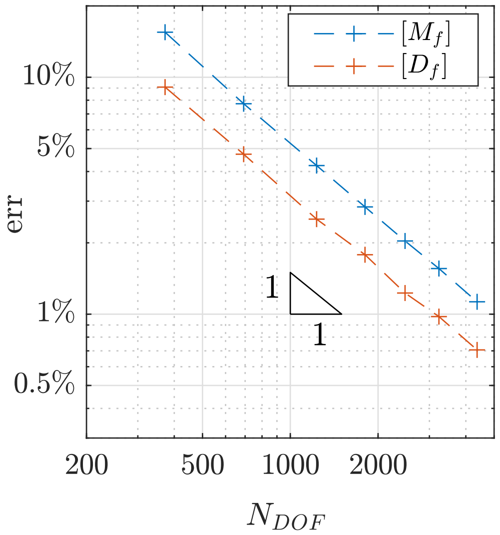

Figure 7: Numerical relative errors (in %) as a function of the number of nodes N_{DOF} associated with the Frobenius norm of the matrices $[M_f^{\mathrm{rig}}]$ and $[G_f^{\mathrm{rig}}]$, revealing a decreasing error in $\mathcal{O}\left(N_{DOF}^{-1}\right)$.

Figure 7 shows a convergence in $\mathcal{O}\left(N_{DOF}^{-1}\right)$, and highlights the validity of the operators written in equations (59). In order to compare with the calculations of Appendix A, the results presented in this section were computed without taking into account the gravity effects ($g = 0$). However, if gravity was to be taken into

L (ellipsoid major axis)	10 m
D (ellipsoid minor axis)	2 m
e (membrane thickness)	1 mm
ρ_f (solid density)	8000 kg.m^{-3}
ν (Poisson's ratio)	0.25
E (Young's modulus)	2× 10^9 Pa
Δp (internal overpressure)	70000 Pa
β (internal fluid compressibility)	0
N_{DOF} (number of mesh nodes)	3037
g (gravity acceleration)	0 ms^{-2}

Table 1: Parameters used for the description of the structure and its internal fluid.

account for a structure with rigid body movements in a fluid of homogeneous density ρ_f, Archimedes' force amplitude and direction would remain constant since the volume of the structure does not change. Hence, it would only add the work of Archimedes' force at order 0, and the rigid body movements would not result in any added stiffness. In order to verify this, the operator $\mathbb{Q}^{\mathrm{T}}[N_{(\bar{p}_\infty)}]\mathbb{Q}$ from equation (59) was computed for the same ellipsoid by taking into account an aerostatic pressure $p_\infty = -\rho_f g \bar{z}$, and the non-dimensional stiffness operator obtained verifies numerically:

$$\frac{\left\|\mathbb{Q}^{\mathrm{T}}[N_{(\bar{p}_\infty)}]\mathbb{Q}\right\|_{\mathrm{fro}}}{\rho_f g L} = \mathcal{O}\left(10^{-4}\right), \tag{71}$$

which seems sufficiently small. Finally, we can consider that the error associated with the numerical approximation of the fluid operators has been quantified and their convergence assessed at least in specific cases. As mentioned in section 2, [6] has shown the symmetry of the added mass and stiffness operators and the skew-symmetry of the gyroscopic operator using the Lagrange equations. This statement is investigated with the operators introduced in this study. In order to do so, the following errors using the Froebenius norm have been determined based on a longitudinal ambient flow $\boldsymbol{u}_\infty$ for the same mesh as in figure 7. The operators have been projected on the arbitrary projection basis $\mathbb{Q}_s$ consisting in the six rigid body movements of space completed by the first flexible (banana shaped) mode of the airship, see section 5 for more details about the projection basis:

$$\frac{\left\|[K_f] - [K_f]^{\mathrm{T}}\right\|_{\mathrm{fro}}}{\|[K_f]\|_{\mathrm{fro}}} = 0.12\%$$

$$\frac{\left\|[G_f] + [G_f]^{\mathrm{T}}\right\|_{\mathrm{fro}}}{\|[G_f]\|_{\mathrm{fro}}} = 0.58\%$$

$$\frac{\left\|[M_f] - [M_f]^{\mathrm{T}}\right\|_{\mathrm{fro}}}{\|[M_f]\|_{\mathrm{fro}}} = 0.02\%.$$

The results above are in agreement with the expected (skew-)symmetry of the operators shown by [6].

5. Stability analysis of a free inflated ellipsoidal membrane

Equations (60) have been developped in time domain. In the test case presented in this section, we will more specifically use the equations in the frequency domain in order to perform a stability analysis on a simple test case, which does not exclude the possibility of application in time domain such as prediction and control in the future [6]. The method introduced in this article is here applied to the particular case of an ellipsoidal inflated membrane in a uniform flow, whose eigenvalues and eigenmodes are computed. The prolate ellipsoid has an aspect ratio of 5 : 1, characterized by the slenderness number $\mathcal{S}$:

$$\mathcal{S} = \frac{L}{D} = 5. \tag{72}$$

In order to characterize the structure, operators $[K_s]$ and $[M_s]$ from equation (60) are calculated using the Finite Element analysis program NASTRAN. For that purpose, a membrane finite element linear model has been used, inflated by an incompressible fluid. Its parameters are described in table 1. The fluid operators $[K_f]$, $[G_f]$ and $[M_f]$ are calculated using the method presented in section 3. Both fluid and solid operators are calculated on the same conforming surface mesh. As mentioned in section 2, the reference interface coincides with the fluid-structure quasi-steady solution. For the sake of simplicity, we calculate in this study the dynamics of the structure as an invariant shape $\overline{\Sigma}$ assuming that the structure quasi-steady state does not drastically change with the value of U_∞. This hypothesis enables us to perform calculations based on the same reference configuration. As a consequence, the structure operators are only computed once, and are associated with a quasi-steady state with no ambient flow (homogeneous external pressure field) used as the reference configuration. The coupled model was obtained by adding the fluid and solid operators as described in equation (60). After characterizing the fluid-structure operators, the objective of this section is to calculate the associated fluid-structure coupled eigenvalues. For this purpose, the displacement $\boldsymbol{\xi}$ is looked for as the product of a function of space $\boldsymbol{q}$ and a function of time:

$$\boldsymbol{\xi}(\boldsymbol{x}, t) = \boldsymbol{q}(\boldsymbol{x})\ \exp(\lambda t), \tag{73}$$

where λ can be complex. In the following, all the variables are written on the reference configuration and the bar notation $\overline{(\bullet)}$ is not used since there is no risk of confusion. The solution in the form of equation (73) is introduced in equation (60), which gives:

$$\Big[([M_s] + [M_f])\,\lambda^2 + [G_f]\,\lambda + [K_s] + [K_f] \Big] \boldsymbol{q} \exp(\lambda t) = 0. \tag{74}$$

However, because the fluid operators are full (as a consequence of condensing the fluid equations on the interface with the integral representation [21]), solving such a problem requires a large amount of memory. To overcome this issue, the size of the problem is reduced by projecting the unknown displacements $\boldsymbol{\xi}$ of the structure on a reduced basis. The basis chosen here contains the six rigid body motions (three translations and three infinitesimal rotations), completed by two structural elastic modes $\boldsymbol{\xi}_7$ and $\boldsymbol{\xi}_8$ (computed with NASTRAN), one of which can be seen on Figure 6. These banana-shaped flexible modes are orthogonal. Both have the same *in vacuo* frequency and only differ by a $\pi/2$ rotation of their direction around the symmetry axis. According to Li et al. [6], these banana modes are expected to be the lowest frequency elastic modes emerging for high aspect ratio flexible airships. The displacement field is therefore projected on a reduced basis $\mathbb{Q}_s$:

$$\boldsymbol{\xi}(\boldsymbol{x}, t) = \mathbb{Q}_s(\boldsymbol{x}) \boldsymbol{q}_s \exp(\lambda t) \tag{75a}$$

$$\text{with } \mathbb{Q}_s = [\mathbb{Q}, \boldsymbol{\xi}_7, \boldsymbol{\xi}_8], \quad \boldsymbol{q}_s = \begin{pmatrix} \boldsymbol{d} \\ \boldsymbol{\theta} \\ q_{s7} \\ q_{s8} \end{pmatrix} \text{ and } [\bullet]_{\mathbb{Q}_s} = \mathbb{Q}_s^{\mathrm{T}} [\bullet] \, \mathbb{Q}_s. \tag{75b}$$

The projection basis $\mathbb{Q}_s$ is an eight-columns concatenation of the rigid body movements matrix $\mathbb{Q}$ defined in (68a) for the first six columns, and the mode shape functions of the bending modes $\boldsymbol{\xi}_7$ and $\boldsymbol{\xi}_8$ for the two last columns. The volume center displacement is given by $\boldsymbol{d}$, the structure rotation is given by $\boldsymbol{\theta}$ and the amplitudes of the elastic modes are given by the modal coefficients q_{s7} and q_{s8}. The displacements are therefore characterized by the new generalized coordinates vector $\boldsymbol{q}_s$ of the fluid-structure problem and the associated eigenvalue λ. Equation (74) is quadratic with respect to λ, however it is much more convenient to determine eigenvalues associated with linear eigen-equations. For that purpose, the equation is shifted

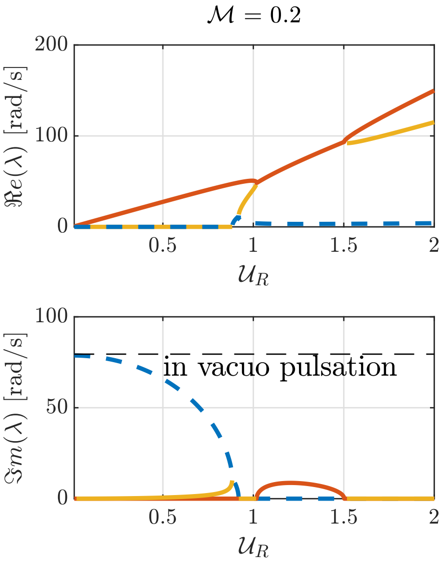

Figure 8: Evolution of the real part of the modes (top) associated with the growth rate and their imaginary part (bottom) associated with the circular frequency as a function of the reduced velocity $\mathcal{U}_R$. The mass ratio is $\mathcal{M} = 0.2$. Each color stands for an identified mode using a Modal Assurance Criterion. Only the modes with positive frequency, positive growth rate and strictly positive absolute value have been plotted. The black horizontal dashed line shows the frequency of the banana mode in the absence of fluid.

into the state space, thus reducing its order in λ from quadratic to linear, which gives by projecting on the $\mathbb{Q}_s$ basis:

$$[M_1]\begin{pmatrix}\boldsymbol{q}_s \\ \lambda\boldsymbol{q}_s\end{pmatrix} = \lambda\,[M_2]\begin{pmatrix}\boldsymbol{q}_s \\ \lambda\boldsymbol{q}_s\end{pmatrix}, \tag{76a}$$

$$\text{with } [M_1] = \begin{bmatrix} 0 & \mathbb{1} \\ [K_s]_{\mathbb{Q}_s} + [K_f]_{\mathbb{Q}_s} & [G_f]_{\mathbb{Q}_s} \end{bmatrix} \text{ and } [M_2]_s = \begin{bmatrix} \mathbb{1} & 0 \\ 0 & -\left([M_s]_{\mathbb{Q}_s} + [M_f]_{\mathbb{Q}_s}\right) \end{bmatrix} \tag{76b}$$

Equation (76a) consists of a system of eight equations since the dynamic equations have been projected on the modal basis with the help of a left-multiplication by $\mathbb{Q}_s^{\mathrm{T}}$. This eigenvalue equation is solved using Matlab for a flow velocity $\boldsymbol{u}_\infty$ colinear to the structure axis. A range of fluid velocities U_∞ and densities ρ_f are investigated. The results are plotted with respect to the reduced velocity $\mathcal{U}_R$ and the mass ratio $\mathcal{M}$ defined as:

$$\mathcal{U}_R = \frac{U_\infty}{\Omega L}, \tag{77a}$$

$$\mathcal{M} = \frac{\rho_f}{\rho_s \frac{e}{D}}. \tag{77b}$$

The reduced velocity $\mathcal{U}_R$ determines the ratio between the flow velocity and the velocity required for a fluid particle to travel across the structure in the time of a characteristic period. The value of the characteristic frequency Ω is chosen as the frequency *in vacuo* of the elastic modes. The mass ratio compares the order of magnitude between the added mass of the fluid and the membrane mass, D being the diameter of the ellipsoid (hence $D = L/5$ for a 5:1 prolate). The particular dependence of the operators on U_∞ is taken advantage of: they are calculated at an arbitrary velocity, and their value can be recalculated for each $\mathcal{U}_R$

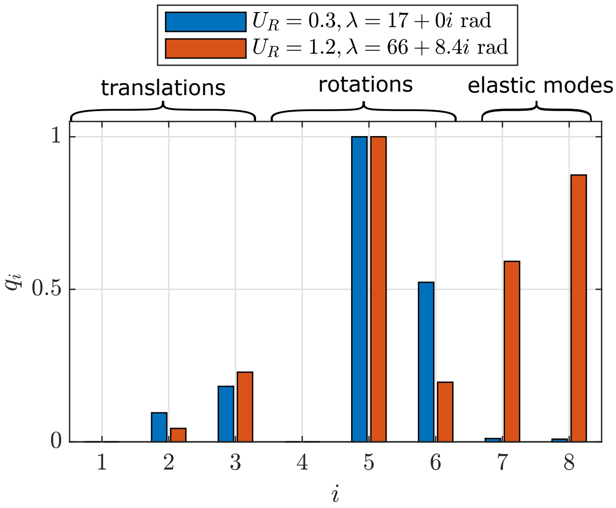

Figure 9: Generalised coordinates of a static unsteady mode (blue) and a flutter mode (orange) for two different values of $\mathcal{U}_R$, with $\mathcal{M} = 0.2$.

with a scalar multiplication, recalling that the mass operator does not vary with U_∞, the gyroscopic operator is linear with U_∞ and the stiffness operator is linear with U_∞^2, as shown in section 3. Similarly, by looking at equation (35) one can deduce that the fluid operators are linear with the fluid density ρ_f.

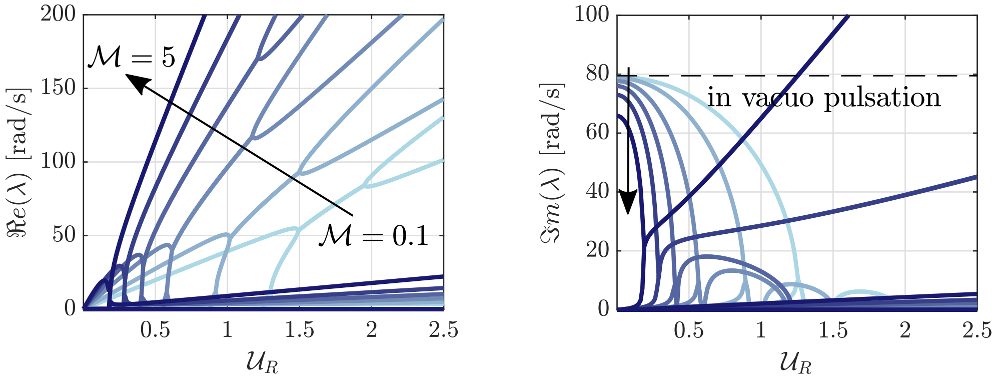

Figure 10: Real part (growth rate, top) and imaginary part (frequency, bottom) of the eigenvalues as a function of the reduced velocity $\mathcal{U}_R$. Curves are for $M = 0.1, 0.2, 0.5, 1, 2$ and 5.

The results are presented Figure 8 for a mass ratio of $\mathcal{M} = 0.2$. The order 0 solution is an unstable equilibrium position as soon as there is a flow because of the absence of fins in this simple test case. Indeed, for $\mathcal{U}_R \in]0, 1]$, the system has a mode with a nil frequency $\Im m(\lambda) = 0$ and a positive growth rate $\Re e(\lambda) > 0$ (plotted in blue in Figure 8): it is a divergence mode. At an arbitrary value $\mathcal{U}_R = 0.3$ in this region, the modal decomposition of this unstable mode $\boldsymbol{q}_s$ is shown in Figure 9 with blue bars. It appears that the generalized coordinates contributing to the instability are the rotations and translations perpendicular to the axis of $\boldsymbol{u}_\infty$, while translation and rotation in the axis of the structure and flexible deformations are not involved in the instability. The latter is triggered by the mechanical moment appearing in equation (A.30b): a small variation of $\boldsymbol{\theta}^1$ induces a moment in the same direction on the structure, leading to an exponentially growing drift. The moment responsible for this drift is known by airship engineers as the Munk moment [1].

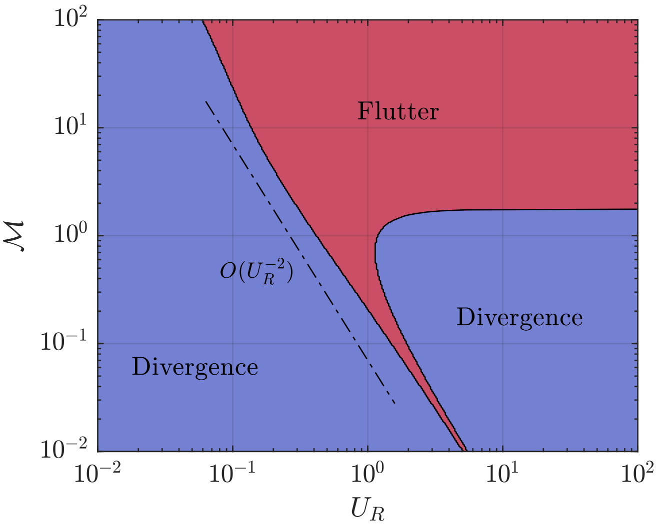

Figure 11: Instability map predicted by the linear model: divergence (static) or flutter (dynamic), for $\mathcal{M} \in [10^{-4}, 10^{6}]$ and $\mathcal{U}_R \in [10^{-2}, 10^{2}]$.

The contribution of the translations displayed in Figure 9 results from the emergence of a force perpendicular to the ambient flow when the structure rotates as predicted by equation (A.30a). In the region $\mathcal{U}_R \in]0, 1]$ of Figure 8, the frequency of the elastic mode (dashed blue line) decreases with the reduced velocity until it vanishes. If the flow velocity increases past this point, another static unstable mode appears (yellow line), with a growth rate increasing with $\mathcal{U}_R$. When the flow reaches the critical velocity $\mathcal{U}_R \simeq 1.04$, the growth rate of the two unstable modes becomes equal, and a coupled mode with a strictly positive frequency and growth rate emerges, resulting in exponentially growing oscillations of the structure. This instability is referred to as post-diverence (or Paidoussis) flutter [30], and is characteristic of conservative gyroscopic systems. This flutter phenomenon is documented in detail in section 3.4 of [30] in the context of clamped pipes conveying fluid. The orange bars from Figure 9 show the generalized coordinates of this flutter mode. It appears that, unlike the static unstable mode below the critical velocity (plotted with blue bars in the same figure), this instability results from the coupling of rigid body movements with elastic deformations of the structure, partly due to the gyroscopic effects of the fluid. Around $\mathcal{U}_R = 1.53$, the flutter mode splits into two static unstable modes. We see as well that for a mass ratio of $\mathcal{M} = 0.2$ the added mass has a low influence on the dynamics. Indeed, for $\mathcal{U}_R = 0$ (hence when fluid stiffness or gyroscopic effects vanish), the frequency of the elastic mode (dashed blue line in Figure 8) is almost the same as the frequency of the structure *in vacuo* (dashed horizontal black line). Figure 10 shows the evolution of the eigenvalues for a range of values of mass ratio $\mathcal{M}$. As expected, for larger values of the fluid density, the frequency of the immersed elastic mode in a fluid at rest decreases.

Figure 11 shows the type of instability of the system (static divergence or flutter) as a function of the parameters $\mathcal{U}_R$ and $\mathcal{M}$. It can be seen that the model presented here provides a quick way to carry out stability studies as a function of flow or structural parameters. We observe that in the absence of fins, the system is always unstable, hence the importance of adding at least a simplified model of the fins like Li [6] to apply the method to real cases.

6. Conclusion

Drawing inspiration from the work of Li et al. [6] to characterize the dynamic aeroelasticity of flexible airships, the method presented in this article aims both to enhance the precision of the prediction of the potential flow effects and to calculate it for various shapes of airships. The approach is based on a linearization of the fluid boundary equation expressed in an ALE formalism, which leads to the numerical calculation of new BEM operators associated to the spatial derivative of the classical BEM operators for a flowing fluid with respect to the structure displacements. After quantifying the numerical and linearization errors associated to the method through test cases, some preliminary results have been presented in section 5, showcasing the advantages of the method for stability analysis of such systems. It also highlighted the high cost of the eigenvalue problem due to the density of the fluid matrices. Though the projection on the dry modal basis helped to overcome this issue, an ongoing development is the use of hierarchical matrices [41] to reduce storage space (currently in $\mathcal{O}\left({N_{DOF}}^2\right)$) and to calculate matrix vector products faster. For applications such as control of trajectory, regarding the rigid body motions, the small displacements hypothesis is a limitation: in order to expand the model to wider flight conditions such as maneuvers, an extension to large displacements coupled with small deformations would be of high interest, as done in works of Thomasson & Woolsey [37] who deal with rigid body motions in currents for example. In order to be able to represent the aspects of lift and drag with the model presented in this article, a solution could be to impose the Kutta condition at the trailing edge of the fins, thus creating a circulation in the flow. For this, it will be necessary to introduce in the integral representation a discontinuity surface (vortex sheet) representing the wake of the airship (as it is done in the panel method, cf [3, 8] for steady flight conditions or by [28] in the case of unsteady, compressible flows but without predicting the linear perturbations around a reference solution). This surface will be discretized by the BEM as it is done for the fluid-structure interface except that the associated operators are hyper-singular, as shown by [21], and their calculation requires more complex mathematical methods such as the algorithm introduced in [42]. This work will be the subject of a future article.

References

[1] Li, Y., Meyer, N. and Sharf, I., 2011, *Airship dynamics modeling: A literature review*, Progress in Aerospace Sciences, 47: 217–239.

[2] Amiryants, G.A., Grigoriev, V.D., Ishmuratov, F.Z., Franz, A., d'Henin, E. and Kaempf, B., 2002, *Investigations of airship aeroelasticity*, 23rd International Congress of Aerospace Sciences, Toronto, Canada.

[3] Bessert, N. and Frederich, O., 2005, *Nonlinear Airship Aeroelasticity*, Journal of Fluids and Structures, 21: 731–742.

[4] J.M. Liu, C.J. Lu, L.P. Xue, 2010, *Numerical investigation on the aeroelastic behavior of an airship with hull-fin configuration*, Journal of Hydrodynamics, 22: 207–213.

[5] Wu, X., Wang, Y., Huang, C., Liu, Y. and Lu, L., 2015, *Experiment and numerical simulation on the characteristics of fluid–structure interactions of non-rigid airships*, Theoretical and Applied Mechanics Letters, 5: 258–261.

[6] Li, Y., Meyer, N. and Sharf, I., 2009, *Dynamics Modeling and Simulation of Flexible Airships*, AIAA Journal, 47: 592—605.

[7] Azouz, N., Chaabani, S., Lerbet, J. and Abichou, A., 2012, *Computation of the added masses of an unconventional airship*, Journal of Applied Mathematics 2012, Article ID 714627.

[8] Lutz, T., Funk, P., Jakobi, S. and Wagner, S., 2002, *Summary of Aerodynamic Studies on the Lotte Airship*, 4th International Airship Convention and Exhibition, Cambridge, England.

[9] Riccardi, G. and De Bernardis, E., 2019, *Numerical simulations of the dynamics and the acoustics of an axisymmetric bubble rising in an inviscid liquid*, European Journal of Mechanics - B/Fluids, 79: 121–140.

[10] van Opstal, T.M., van Brummelen, E.H., de Borst, R. and Lewis, M., 2012, *A finite-element/boundary-element method for large-displacement fluid–structure interaction with potential flow*, Computer Methods in Applied Mechanics and Engineering, 50(6): 779–788.

[11] Tan, K. L., Khoo, B. C. and White, J. K., 2008, *A level set–boundary element method for the simulation of underwater bubble dynamics*, SIAM Journal on Scientific Computing, 30(2): 549–571.

[12] Garzon, M., Adalsteinsson, D., Gray, L. and Sethian, J. A., 2005, *A coupled level set–boundary integral method for moving boundary simulations*, Interfaces and Free Boundaries, 7: 277–302.

[13] Veron, E. and Bouzidi, R., 2016, *Large displacements of light thin flexible structures coupled with heavy fluids using co-simulation between finite element and fast boundary element solvers*, Proceedings of the 11th International Conference on Flow-Induced Vibration, The Hague, The Netherlands.

[14] Schotté, J.-S., Doaré, O., Le Mestre, R., 2019, *Effect of coupling with internal and external fluids on the mechanical behaviour of aerostats*, 7th International Conference on Structural Engineering, Mechanics and Computation, Cape Town, South Africa.

[15] Folland, G.B., 1995, *Introduction to partial differential equations* (Vol. 102), Princeton university press.

[16] Morand, H. J.-P., and Ohayon, R., 1995, Fluid structure interaction-Applied numerical methods, Wiley.

[17] Pfister, J.-L., Marquet, O. and Carini, M., 2019, *Linear stability analysis of strongly coupled fluid–structure problems with the Arbitrary-Lagrangian–Eulerian method*, Computer Methods in Applied Mechanics and Engineering, 355: 663—689.

[18] Ciarlet, P.G., 2005, *An introduction to differential geometry with applications to elasticity*, Journal of elasticity, 78(1): 1–215

[19] Haug, E.-J., Choi, K.-K and Komkov, V., 1986, *Design sensitivity analysis of structural systems*, Elsevier Science.

[20] Henrot, A. and Pierre, M., 2005, *Variation et optimisation de formes*, Springer.

[21] Bonnet, M., 1999, *Boundary integral equation methods for solids and fluids*, Wiley.

[22] Hughes, T., Liu, W. and Zimmermann, T., 1981, *Lagrangian-Eulerian finite element formulation for incompressible viscous flows.* Computer Methods in Applied Mechanics and Engineering, 29: 329–349.

[23] Veron, E., 2016, *Calcul numérique des grandes déformations de structures minces en contact avec des fluides lourds* (*Numerical simulation of large displacements of thin flexible structures coupled with heavy fluids*), Doctoral dissertation, Nantes.

[24] Theodorsen, T., 1949, *General theory of aerodynamic instability and the mechanism of flutter*, NACA Technical Report 496.

[25] Dowell, E. H., 1989, *A modern course in aeroelasticity*, Eds. Howard C. Curtiss, Robert H. Scanlan, and Fernando Sisto. Vol. 3. Dordrecht, The Netherlands: Kluwer academic publishers.

[26] Potthast, R., 1994, *Fréchet differentiability of boundary integral operators in inverse acoustic scattering*, Inverse Problems, 10(2): 64–84.

[27] John, D. and Anderson, D., 2003, *Modern compressible flow*, Mc Graw Hill.

[28] Gennaretti, M., Luceri, L. and Morino, L., 1997, *A unified boundary integral methodology for aerodynamics and aeroacoustics of rotors*, Journal of Sound and Vibration, 200(4): 467–489.

[29] Ziegler, H., 2013, *Principles of structural stability*, Birkhäuser.

[30] Paidoussis, M. P., 1998, *Fluid-structure interactions: slender structures and axial flow*, Volume 1, Academic press.

[31] Destuynder, P. and Santi, F. 2006, *A progressive Euler-Lagrange formulation for aeroelasticity model of quasi-axisymmetrical airship*, ECCOMAS CFD 2006: proceedings of the European Conference on Computational Fluid Dynamics.

[32] Pozrikidis, C., 2002, *A practical guide to boundary element methods with the software library BEMLIB*, CRC Press.

[33] Fischnaller, H. and Thöbin K., 2009, *Numerical integration - an introduction to the Boundary Element Method*, Masters project for Graz unitersity of technology.

[34] Katz, J. and Plotkin, A., 2001, *Low-speed aerodynamics*, Cambridge university press, Vol. 13.

[35] Rangette, A., 1990, *A boundary element method to calculate the fluid hydrodynamic mass matrix in structural analysis including free surface waves*, Engineering Computations, 7(3): 210–216.

[36] Lamb, H., 1924, *Hydrodynamics*, University Press.

[37] Thomasson, P. G. and Woolsey, C. A., 2013, *Vehicle motion in currents*, IEEE Journal of Oceanic Engineering, 38(2): 226–242.

[38] Clarke, D.B., 2009, *Experimental and computational investigation of flow about low aspect ratio ellipsoids at transcritical Reynolds numbers, Appendix C*, Doctoral dissertation, University of Tasmania.

[39] Lamb, H., 1918, *The inertia coefficients of an ellipsoid moving in fluid*, Reports and memoranda, 128–129.

[40] De Langre, E., 2008. *Effects of wind on plants*, Annual Reviews of Fluid Mechanics, 40: 141–168.

[41] Chaillat, S., Desiderio, L., Ciarlet, P., 2017, *Theory and implementation of $\mathcal{H}$-matrix based iterative and direct solvers for Helmholtz and elastodynamic oscillatory kernels*, Journal of Computational Physics, 351: 165—186.

[42] Guiggiani, M., Krishnasamy, G., Rudolphi, T. J. and Rizzo, F.J., 1992, *A general algorithm for the numerical solution of hypersingular boundary integral equations*, Journal of Applied Mechanics, 59(3): 604–614.

Appendix A. Detailed calculation of the linearization

We detail here how the linearization was performed.

Linearized Green's function

The order 1 Taylor expansion of the norm of a vector $\boldsymbol{a}$ at an arbitrary power n is:

$$\|\boldsymbol{a}\|^n = \left\|\boldsymbol{a}^0\right\|^n + \boldsymbol{a}^0 \cdot \boldsymbol{a}^1 \left\|\boldsymbol{a}^0\right\|^{n-2} + \mathcal{O}\left(\varepsilon^2\right), \tag{A.1}$$

allowing to calculate the following formula:

$$\|\boldsymbol{x}-\boldsymbol{y}\|^n = \|\bar{\boldsymbol{x}}-\bar{\boldsymbol{y}}\|^n + n(\bar{\boldsymbol{x}}-\bar{\boldsymbol{y}}) \cdot \left(\boldsymbol{\xi}^1_{(\bar{\boldsymbol{x}})} - \boldsymbol{\xi}^1_{(\bar{\boldsymbol{y}})}\right) \|\bar{\boldsymbol{x}}-\bar{\boldsymbol{y}}\|^{n-2} + \mathcal{O}\left(\varepsilon^2\right) \quad \text{on } \overline{\Sigma}. \tag{A.2}$$

The Green's function given by (19) and its gradient becomes, when combined with the linearized expression (A.2):

$$\overline{\boldsymbol{G_n}}^0 = -\frac{1}{4\pi}\frac{\bar{\boldsymbol{n}}}{\|\bar{\boldsymbol{x}}-\bar{\boldsymbol{y}}\|} \tag{A.3a}$$

$$\overline{\boldsymbol{G_n}}^1 = \frac{1}{4\pi}\left(\frac{(\bar{\boldsymbol{x}}-\bar{\boldsymbol{y}})\cdot\left(\boldsymbol{\xi}^1_{(\bar{\boldsymbol{x}})}-\boldsymbol{\xi}^1_{(\bar{\boldsymbol{y}})}\right)\bar{\boldsymbol{n}}}{\|\bar{\boldsymbol{x}}-\bar{\boldsymbol{y}}\|^3} - \frac{\bar{\boldsymbol{\tau}}^1}{\|\bar{\boldsymbol{x}}-\bar{\boldsymbol{y}}\|}\right) \tag{A.3b}$$

$$\overline{\partial_n G}^0 = \frac{1}{4\pi}\frac{(\bar{\boldsymbol{x}}-\bar{\boldsymbol{y}})\cdot\bar{\boldsymbol{n}}}{\|\boldsymbol{x}-\boldsymbol{y}\|^3} \tag{A.3c}$$

$$\overline{\partial_n G}^1 = \frac{1}{4\pi}\left(\frac{(\bar{\boldsymbol{x}}-\bar{\boldsymbol{y}})\cdot\bar{\boldsymbol{\tau}}^1}{\|\boldsymbol{x}-\boldsymbol{y}\|^3} + \frac{\left(\boldsymbol{\xi}^1_{(\bar{\boldsymbol{x}})}-\boldsymbol{\xi}^1_{(\bar{\boldsymbol{y}})}\right)\cdot\bar{\boldsymbol{n}}}{\|\bar{\boldsymbol{x}}-\bar{\boldsymbol{y}}\|^3}\right. \tag{A.3d}$$

$$\left. - 3\frac{(\bar{\boldsymbol{x}}-\bar{\boldsymbol{y}})\cdot\left(\boldsymbol{\xi}^1_{(\bar{\boldsymbol{x}})}-\boldsymbol{\xi}^1_{(\bar{\boldsymbol{y}})}\right)(\bar{\boldsymbol{x}}-\bar{\boldsymbol{y}})\cdot\bar{\boldsymbol{n}}}{\|\bar{\boldsymbol{x}}-\bar{\boldsymbol{y}}\|^5}\right). \tag{A.3e}$$

Linearized flow velocity

In order to express the linear variations of the flow velocity at order ε on the interface, recalling that

$$\boldsymbol{u} = \boldsymbol{\nabla}\phi = \frac{\partial\phi}{\partial\boldsymbol{x}}, \tag{A.4}$$

one can express on the reference interface with the chain rule:

$$\begin{aligned}\bar{\boldsymbol{u}} &= \frac{\partial\bar{\boldsymbol{x}}}{\partial\boldsymbol{x}}\frac{\partial\bar{\phi}}{\partial\bar{\boldsymbol{x}}}\\ &= \left(\frac{\partial\boldsymbol{x}}{\partial\bar{\boldsymbol{x}}}\right)^{-\mathrm{T}}\overline{\boldsymbol{\nabla}}\bar{\phi}\\ &= (\mathbb{1}+\overline{\nabla}\boldsymbol{\xi})^{-\mathrm{T}}\overline{\boldsymbol{\nabla}}\bar{\phi}.\end{aligned} \tag{A.5}$$

The linearized inversion of the terms in the parentheses of the above equation enables to write at both orders of magnitude 0 and ε:

$$\bar{\boldsymbol{u}} = \overline{\boldsymbol{\nabla}}\bar{\phi}^0 + \overline{\boldsymbol{\nabla}}\bar{\phi}^1 - \left[\overline{\nabla}^{\mathrm{T}}\boldsymbol{\xi}^1\right]\overline{\boldsymbol{\nabla}}\bar{\phi}^0 + \mathcal{O}\left(\varepsilon^2\right), \tag{A.6}$$

hence the demonstration of (46).

Linearized quadratic flow velocity

The linearized term $\bar{\boldsymbol{u}}^0.\bar{\boldsymbol{u}}^1$ is developed into a more useful formulation. Because of the non penetration condition (10) at order 0:

$$\bar{\boldsymbol{u}}^0\cdot\bar{\boldsymbol{n}} = 0 \quad \text{on } \overline{\Sigma}, \tag{A.7}$$

by introducing the tangential and normal components of any arbitrary vector $\bar{\boldsymbol{a}}$ on $\overline{\Sigma}$:

$$\begin{aligned}\bar{\boldsymbol{a}}_n &= (\bar{\boldsymbol{n}}\otimes\bar{\boldsymbol{n}})\bar{\boldsymbol{a}}\\ \bar{\boldsymbol{a}}_S &= \bar{\boldsymbol{a}}-\bar{\boldsymbol{a}}_n\\ \bar{\boldsymbol{a}} &= \bar{\boldsymbol{a}}_S+\bar{\boldsymbol{a}}_n,\end{aligned} \tag{A.8}$$

we obtain:

$$\bar{\boldsymbol{u}}^0 = \bar{\boldsymbol{u}}^0_S \quad \text{on } \overline{\Sigma}. \tag{A.9}$$

The scalar product becomes

$$\begin{aligned}\bar{\boldsymbol{u}}^0 \cdot \bar{\boldsymbol{u}}^1 &= \bar{\boldsymbol{u}}^0_S \cdot (\bar{\boldsymbol{u}}^1_S + \bar{\boldsymbol{u}}^1_n) \\ &= \bar{\boldsymbol{u}}^0_S \cdot \bar{\boldsymbol{u}}^1_S \quad \text{on } \overline{\Sigma}.\end{aligned} \tag{A.10}$$

Using equation (46), we obtain:

$$\bar{\boldsymbol{u}}^1_S = (1 - \bar{\boldsymbol{n}} \otimes \bar{\boldsymbol{n}}) \left(\overline{\boldsymbol{\nabla}}\bar{\phi}^1 - \left(\overline{\nabla}^{\mathrm{T}}\bar{\boldsymbol{\xi}}^1 \bar{\boldsymbol{u}}^0\right)\right) = \overline{\boldsymbol{\nabla}}_S \bar{\phi}^1 - (\overline{\nabla}_S^{\mathrm{T}} \bar{\boldsymbol{\xi}}^1)\bar{\boldsymbol{u}}^0 \quad \text{on } \overline{\Sigma}. \tag{A.11}$$

By combining equations (A.10) and (A.11) we obtain:

$$\bar{\boldsymbol{u}}^0 \cdot \bar{\boldsymbol{u}}^1 = \bar{\boldsymbol{u}}^0 \cdot \left(\overline{\boldsymbol{\nabla}}_S \bar{\phi}^1 - \overline{\nabla}_S^{\mathrm{T}} \bar{\boldsymbol{\xi}}^1 \bar{\boldsymbol{u}}^0\right) \quad \text{on } \overline{\Sigma}. \tag{A.12}$$

Linearized velocity

It might be of interest, in order to validate the code for example, to be able to calculate the fluid velocity at the interface. The velocity can be decomposed into a surface and a normal component, since the surface gradient of the potential is calculated more conveniently than its total gradient since the potential is calculated only at the interface with the BEM:

$$\boldsymbol{u} = \boldsymbol{u}_S + (\boldsymbol{n} \otimes \boldsymbol{n})\boldsymbol{u} \quad \text{on } \Sigma_{(t)} \tag{A.13}$$

where it is important to notice that $\boldsymbol{u}_S = \boldsymbol{\nabla}_S \phi$ is calculated with the surface gradient in the deformed configuration:

$$\boldsymbol{\nabla}_S \phi = (\mathbb{1} - \boldsymbol{n} \otimes \boldsymbol{n})\, \boldsymbol{\nabla} \phi \quad \text{on } \Sigma_{(t)}. \tag{A.14}$$

By developing at order ε the above equation:

$$\boldsymbol{\nabla}_S \phi = (\mathbb{1} - \bar{\boldsymbol{n}} \otimes \bar{\boldsymbol{n}})\overline{\boldsymbol{\nabla}}\bar{\phi}^0 - (\bar{\boldsymbol{n}} \otimes \boldsymbol{n}^1 + \boldsymbol{n}^1 \otimes \bar{\boldsymbol{n}})\overline{\boldsymbol{\nabla}}\bar{\phi}^0 - \overline{\nabla}_S^{\mathrm{T}} \bar{\boldsymbol{\xi}}^1 \overline{\boldsymbol{\nabla}}_S \bar{\phi}^0 + \overline{\boldsymbol{\nabla}}_S \bar{\phi}^1 + \mathcal{O}\left(\varepsilon^2\right) \quad \text{on } \Sigma_{(t)}. \tag{A.15}$$

Therefore, we obtain the steady velocity at orders 0 and 1 by combining equations (38a) and (A.15):

$$\begin{aligned}\bar{\boldsymbol{u}}^0_S &= (\mathbb{1} - \bar{\boldsymbol{n}} \otimes \bar{\boldsymbol{n}})\, \overline{\boldsymbol{\nabla}}\bar{\phi}^0 = \overline{\boldsymbol{\nabla}}_S \bar{\phi}^0 && \text{on } \overline{\Sigma}, \\ \bar{\boldsymbol{u}}^1_S &= \overline{\boldsymbol{\nabla}}_S \bar{\phi}^1 - \left(\left(\overline{\nabla}_S^{\mathrm{T}} \bar{\boldsymbol{\xi}}^1 \bar{\boldsymbol{n}}\right) \otimes \bar{\boldsymbol{n}} + \bar{\boldsymbol{n}} \otimes \left(\overline{\nabla}_S^{\mathrm{T}} \bar{\boldsymbol{\xi}}^1 \bar{\boldsymbol{n}}\right) - \overline{\nabla}_S^{\mathrm{T}} \bar{\boldsymbol{\xi}}^1\right) \overline{\nabla}_S \bar{\phi}^0 && \text{on } \overline{\Sigma}.\end{aligned} \tag{A.16}$$

It has been noted that the first line had already been determined in equation (46) since the small displacements of the structure only affect the order $\mathcal{O}(\varepsilon)$ of the solution. Because the surface gradient is perpendicular to the normal, the expression at order 1 can be further simplified with:

$$\bar{\boldsymbol{u}}^1_S = \overline{\boldsymbol{\nabla}}_S \bar{\phi}^1 - \left(\bar{\boldsymbol{n}} \otimes \left(\overline{\nabla}_S^{\mathrm{T}} \bar{\boldsymbol{\xi}}^1 \bar{\boldsymbol{n}}\right) - \overline{\nabla}_S^{\mathrm{T}} \bar{\boldsymbol{\xi}}^1\right) \overline{\nabla}_S \bar{\phi}^0 \quad \text{on } \overline{\Sigma}. \tag{A.17}$$

By multiplying the boundary condition (10) with the normal, one gets:

$$(\boldsymbol{n} \otimes \boldsymbol{n})\boldsymbol{u} = (\boldsymbol{n} \otimes \boldsymbol{n})\frac{\partial \boldsymbol{\xi}}{\partial t} = (\bar{\boldsymbol{n}} \otimes \bar{\boldsymbol{n}})\frac{\partial \bar{\boldsymbol{\xi}}^1}{\partial t} + \mathcal{O}\left(\varepsilon^2\right) \quad \text{on } \Sigma_{(t)} \tag{A.18}$$

By combining equations (A.13), (A.17) and (A.18), the order 1 fluctuations of the velocity are obtained:

$$\boldsymbol{u}^1 = \overline{\boldsymbol{\nabla}}_S \bar{\phi}^1 - \left(\bar{\boldsymbol{n}} \otimes \left(\overline{\nabla}_S^{\mathrm{T}} \bar{\boldsymbol{\xi}}^1 \bar{\boldsymbol{n}}\right) - \overline{\nabla}_S^{\mathrm{T}} \bar{\boldsymbol{\xi}}^1\right) \overline{\nabla}_S \bar{\phi}^0 + (\bar{\boldsymbol{n}} \otimes \bar{\boldsymbol{n}})\frac{\partial \bar{\boldsymbol{\xi}}^1}{\partial t} \quad \text{on } \overline{\Sigma}. \tag{A.19}$$

Linearized rigid-body gyroscopic loads

In order to validate the linearized equations of our model, this appendix displays here the exact nonlinear work from the pressure of an inviscid and irrotational fluid on a rigid structure. The efforts depending on the 6 rigid body movements will then be linearized in order to introduce a formulation with a fluid stiffness, damping and mass, allowing to compare the numerical results of section 4 with the analytical results displayed here. In order to parameterize the rigid body movements of the structure, the displacements are decomposed into a translation $\boldsymbol{d}$ and a rotation $\boldsymbol{\theta}$ such that:

$$\bar{\boldsymbol{\xi}}^1 = \bar{\boldsymbol{d}}^1 + \bar{\boldsymbol{\theta}}^1_\times \bar{\boldsymbol{x}}, \tag{A.20}$$

where the subscript × on a vector denotes the 3×3 matrix associated with the cross product × such that

$$\bar{\boldsymbol{\theta}}_\times \bar{\boldsymbol{x}} = \bar{\boldsymbol{\theta}} \times \bar{\boldsymbol{x}}. \tag{A.21}$$

The frame attached to the structure is noted $\tilde{\Sigma}$, which is equal to the reference frame $\overline{\Sigma}$ which has been rotated by the rotation operator $\mathbb{R}$ defined in equation (A.22a). First, literature gives the analytic expression of the 6×6 added mass matrix $[M_f^{\text{rig}}]$ of a revolution ellipsoid for any major to minor axis aspect ratio. Secondly, one can find the dynamical force and moment ($\tilde{\boldsymbol{F}}_{F/S}$ and $\tilde{\boldsymbol{M}}_{F/S}$ respectively) for a perfect stationary homogeneous ambient flow on a structure in a rigid body motion described by a velocity $\tilde{\boldsymbol{v}}$ at the center of volume and a rate of rotation $\tilde{\boldsymbol{\omega}}$. The tilde notation $(\tilde{\bullet})$ is associated with the expression of an array in the body frame, which is linked to the expression on the reference interface with the rotation operator $\mathbb{R}$ associated with a rotation angle of the structure $\boldsymbol{\theta}$:

$$\mathbb{R} = \mathbb{1} + \bar{\boldsymbol{\theta}}^1_\times + \mathcal{O}\left(\varepsilon^2\right), \tag{A.22a}$$

$$(\tilde{\bullet}) = \mathbb{R}^{-1}(\bar{\bullet}). \tag{A.22b}$$

The expression of the potential force and moment in the case of rigid body movements of a structure can be found in [37]:

$$\begin{pmatrix} \tilde{\boldsymbol{F}}_{F/S} \\ \tilde{\boldsymbol{M}}_{F/S} \end{pmatrix} = -\left[M_f^{\text{rig}}\right] \begin{pmatrix} \frac{\mathrm{d}\tilde{\boldsymbol{v}}}{\mathrm{d}t} - (\tilde{\boldsymbol{u}}_\infty)_\times \tilde{\boldsymbol{\omega}} \\ \frac{\mathrm{d}\tilde{\boldsymbol{\omega}}}{\mathrm{d}t} \end{pmatrix} - \begin{bmatrix} \tilde{\boldsymbol{\omega}}_\times & (0) \\ (\tilde{\boldsymbol{v}} - \tilde{\boldsymbol{u}}_\infty)_\times & \tilde{\boldsymbol{\omega}}_\times \end{bmatrix} \left[M_f^{\text{rig}}\right] \begin{pmatrix} \tilde{\boldsymbol{v}} - \tilde{\boldsymbol{u}}_\infty \\ \tilde{\boldsymbol{\omega}} \end{pmatrix}. \tag{A.23}$$

In the case of an ellipsoid, the added mass matrix $\left[M_f^{\text{rig}}\right]$ has only diagonal terms and can therefore be rewritten on the form:

$$\left[M_f^{\text{rig}}\right] = \begin{bmatrix} [M_{f1}] & (0) \\ (0) & [M_{f2}] \end{bmatrix}, \tag{A.24}$$

enabling to develop the expression of the force and moment:

$$\tilde{\boldsymbol{F}}_{F/S} = -\left[M_{f1}\right]\left(\frac{\mathrm{d}\tilde{\boldsymbol{v}}}{\mathrm{d}t} - (\tilde{\boldsymbol{u}}_\infty)_\times \tilde{\boldsymbol{\omega}}\right) - \tilde{\boldsymbol{\omega}}_\times \left[M_{f1}\right](\tilde{\boldsymbol{v}} - \tilde{\boldsymbol{u}}_\infty) \tag{A.25a}$$

$$\tilde{\boldsymbol{M}}_{F/S} = -\left[M_{f2}\right]\frac{\mathrm{d}\tilde{\boldsymbol{\omega}}}{\mathrm{d}t} - (\tilde{\boldsymbol{v}} - \tilde{\boldsymbol{u}}_\infty)_\times \left[M_{f1}\right](\tilde{\boldsymbol{v}} - \tilde{\boldsymbol{u}}_\infty) - \tilde{\boldsymbol{\omega}}_\times \left[M_{f2}\right]\tilde{\boldsymbol{\omega}} \tag{A.25b}$$

Since the structure has rotated, the relative direction of the ambient flow varies as follows:

$$\tilde{\boldsymbol{u}}_\infty = \mathbb{R}^{-1}\bar{\boldsymbol{u}}_\infty = \left(\mathbb{1} - \bar{\boldsymbol{\theta}}^1_\times\right)\bar{\boldsymbol{u}}_\infty + \mathcal{O}\left(\varepsilon^2\right), \tag{A.26}$$

and similarly for the other vectors associated with the kinematics, we have $\tilde{\boldsymbol{\omega}}^1 = \bar{\boldsymbol{\omega}}^1 + \mathcal{O}\left(\varepsilon^2\right)$, $\tilde{\boldsymbol{v}}^1 = \bar{\boldsymbol{v}}^1 + \mathcal{O}\left(\varepsilon^2\right)$, and the same goes for the time derivatives of $\tilde{\boldsymbol{v}}^1$. The linearized expression of the force and moment in the reference frame is:

$$\begin{pmatrix} \bar{\boldsymbol{F}}_{F/S} \\ \bar{\boldsymbol{M}}_{F/S} \end{pmatrix} = \left(\mathbb{1} + \bar{\boldsymbol{\theta}}^1_\times\right) \begin{pmatrix} \tilde{\boldsymbol{F}}_{F/S} \\ \tilde{\boldsymbol{M}}_{F/S} \end{pmatrix} + \mathcal{O}\left(\varepsilon^2\right). \tag{A.27}$$

we get the new expression of the fluid forces depending on the displacement of the structure and its time derivatives on the reference domain:
Therefore, by combining equations (A.25), (A.26) and (Appendix A) we obtain the expression of the fluid forces

$$\bar{\boldsymbol{F}}_{F/S} = -\left[M_{f1}\right]\left(\frac{\mathrm{d}\bar{\boldsymbol{v}}^1}{\mathrm{d}t} - \left(\left(\mathbb{1} - \bar{\boldsymbol{\theta}}^1_\times\right)\bar{\boldsymbol{u}}_\infty\right)_\times \bar{\boldsymbol{\omega}}^1\right) - \bar{\boldsymbol{\omega}}^1_\times\left[M_{f1}\right]\left(\bar{\boldsymbol{v}}^1 - \left(\mathbb{1} - \bar{\boldsymbol{\theta}}^1_\times\right)\bar{\boldsymbol{u}}_\infty\right) + \mathcal{O}\left(\varepsilon^2\right), \tag{A.28a}$$

$$\begin{aligned} \bar{\boldsymbol{M}}_{F/S} = &-\left[M_{f2}\right]\left(\frac{\mathrm{d}\bar{\boldsymbol{\omega}}^1}{\mathrm{d}t}\right) - \left(\mathbb{1} + \bar{\boldsymbol{\theta}}^1_\times\right)\left(\bar{\boldsymbol{v}}^1 - \left(\mathbb{1} - \bar{\boldsymbol{\theta}}^1_\times\right)\bar{\boldsymbol{u}}_\infty\right)_\times\left[M_{f1}\right]\left(\bar{\boldsymbol{v}}^1 - \left(\mathbb{1} - \bar{\boldsymbol{\theta}}^1_\times\right)\bar{\boldsymbol{u}}_\infty\right) + \ldots \\ &\bar{\boldsymbol{\omega}}^1_\times\left[M_{f1}\right]\bar{\boldsymbol{\omega}}^1 + \mathcal{O}\left(\varepsilon^2\right). \end{aligned} \tag{A.28b}$$

which becomes by expanding the terms:

$$\bar{\boldsymbol{F}}_{F/S} = -\left[M_{f1}\right]\left(\frac{\mathrm{d}\bar{\boldsymbol{v}}^1}{\mathrm{d}t} - \left(\bar{\boldsymbol{u}}_\infty\right)_\times\bar{\boldsymbol{\omega}}^1\right) + \bar{\boldsymbol{\omega}}^1_\times\left[M_{f1}\right]\bar{\boldsymbol{u}}_\infty \tag{A.29a}$$

$$\begin{aligned} \bar{\boldsymbol{M}}_{F/S} = &-\left[M_{f2}\right]\left(\frac{\mathrm{d}\bar{\boldsymbol{\omega}}^1}{\mathrm{d}t}\right) + \bar{\boldsymbol{v}}^1_\times\left[M_{f1}\right]\bar{\boldsymbol{u}}_\infty + \left(\bar{\boldsymbol{u}}_\infty\right)_\times\left[M_{f1}\right]\bar{\boldsymbol{v}}^1 + \left(\bar{\boldsymbol{\theta}}^1_\times\bar{\boldsymbol{u}}_\infty\right)_\times\left[M_{f1}\right]\bar{\boldsymbol{u}}_\infty + \ldots \\ &\left(\bar{\boldsymbol{u}}_\infty\right)_\times\left[M_{f1}\right]\left(\bar{\boldsymbol{\theta}}^1_\times\bar{\boldsymbol{u}}_\infty\right) - \left(\bar{\boldsymbol{u}}_\infty\right)_\times\left[M_{f1}\right]\bar{\boldsymbol{u}}_\infty - \bar{\boldsymbol{\theta}}^1_\times\left(\bar{\boldsymbol{u}}_\infty\right)_\times\left[M_{f1}\right]\bar{\boldsymbol{u}}_\infty. \end{aligned} \tag{A.29b}$$

In order to get an expression in the form of stiffness, damping and mass operators appear, we switch the position of the variables using the skew-symmetry properties of the cross product:

$$\bar{\boldsymbol{F}}_{F/S} = -\left[M_{f1}\right]\left(\frac{\mathrm{d}\bar{\boldsymbol{v}}^1}{\mathrm{d}t} - \left(\bar{\boldsymbol{u}}_\infty\right)_\times\bar{\boldsymbol{\omega}}^1\right) - \left(\left[M_{f1}\right]\bar{\boldsymbol{u}}_\infty\right)_\times\bar{\boldsymbol{\omega}}^1 \tag{A.30a}$$

$$\begin{aligned} \bar{\boldsymbol{M}}_{F/S} = &-\left[M_{f2}\right]\left(\frac{\mathrm{d}\bar{\boldsymbol{\omega}}^1}{\mathrm{d}t}\right) - \left(\left[M_{f1}\right]\bar{\boldsymbol{u}}_\infty\right)_\times\bar{\boldsymbol{v}}^1 + \left(\bar{\boldsymbol{u}}_\infty\right)_\times\left[M_{f1}\right]\bar{\boldsymbol{v}}^1 + \left(\left[M_{f1}\right]\bar{\boldsymbol{u}}_\infty\right)_\times\left(\bar{\boldsymbol{u}}_\infty\right)_\times\bar{\boldsymbol{\theta}}^1 - \ldots \\ &\left(\bar{\boldsymbol{u}}_\infty\right)_\times\left[M_{f1}\right]\left(\bar{\boldsymbol{u}}_\infty\right)_\times\bar{\boldsymbol{\theta}}^1 - \left(\bar{\boldsymbol{u}}_\infty\right)_\times\left[M_{f1}\right]\bar{\boldsymbol{u}}_\infty + \left(\left(\bar{\boldsymbol{u}}_\infty\right)_\times\left[M_{f1}\right]\bar{\boldsymbol{u}}_\infty\right)_\times\bar{\boldsymbol{\theta}}^1. \end{aligned} \tag{A.30b}$$

By rearranging the terms in a suitable way, the above equation can be rewritten as

$$\begin{pmatrix} \bar{\boldsymbol{F}}_{F/S} \\ \bar{\boldsymbol{M}}_{F/S} \end{pmatrix}^0 = -\begin{pmatrix} \boldsymbol{0} \\ \left(\bar{\boldsymbol{u}}_\infty\right)_\times\left[M_{f1}\right]\bar{\boldsymbol{u}}_\infty \end{pmatrix} \tag{A.31a}$$

$$\begin{pmatrix} \bar{\boldsymbol{F}}_{F/S} \\ \bar{\boldsymbol{M}}_{F/S} \end{pmatrix}^1 = -\left[M_f^{rig}\right]\begin{pmatrix} \frac{d\bar{\boldsymbol{v}}}{dt}^1 \\ \frac{d\bar{\boldsymbol{\omega}}}{dt}^1 \end{pmatrix} - \left[G_f^{rig}\right]\begin{pmatrix} \bar{\boldsymbol{v}}^1 \\ \bar{\boldsymbol{\omega}}^1 \end{pmatrix} - \left[K_f^{rig}\right]\begin{pmatrix} \bar{\boldsymbol{d}}^1 \\ \bar{\boldsymbol{\theta}}^1 \end{pmatrix}, \tag{A.31b}$$

$$\left[G_f^{rig}\right] = \begin{bmatrix} (0) & \left(\left[M_{f1}\right]\bar{\boldsymbol{u}}_\infty\right)_\times - \left[M_{f1}\right]\left(\bar{\boldsymbol{u}}_\infty\right)_\times \\ \left(\left[M_{f1}\right]\bar{\boldsymbol{u}}_\infty\right)_\times - \left(\bar{\boldsymbol{u}}_\infty\right)_\times\left[M_{f1}\right] & (0) \end{bmatrix}, \tag{A.31c}$$

$$\left[K_f^{rig}\right] = \begin{bmatrix} (0) & (0) \\ (0) & \left(\bar{\boldsymbol{u}}_\infty\right)_\times\left[M_{f1}\right]\left(\bar{\boldsymbol{u}}_\infty\right)_\times - \left(\left[M_{f1}\right]\bar{\boldsymbol{u}}_\infty\right)_\times\left(\bar{\boldsymbol{u}}_\infty\right)_\times - \left(\left(\bar{\boldsymbol{u}}_\infty\right)_\times\left[M_{f1}\right]\bar{\boldsymbol{u}}_\infty\right)_\times \end{bmatrix}, \tag{A.31d}$$

where the displacement of the structure $\bar{\boldsymbol{d}}^1$ has been artificially introduced in order to obtain arrays of variables at order ε linked with a temporal derivatives, even though the displacement does not intervene in the dynamics of the structure since the problem is invariant by translation, which is in agreement with the factors of $\bar{\boldsymbol{d}}^1$ being all nil in the above equation.